Journal of Geochemical Exploration 180 (2017) 35–51

Contents lists available at ScienceDirect

Journal of Geochemical Exploration

journal homepage: www.elsevier.com/locate/gexplo

Lithogeochemistry and chemostratigraphy of the Rosemont Cu-Mo-Ag skarn deposit, SE Tucson Arizona: A simplicial geometry approach

Juan C. Ordóñez-Calderón[a,b,*], Sergio Gelcich[a], Faiqa Fiaz[a]

[a] Hudbay, Suite 800, 25 York Street, Toronto, Ontario, Canada
[b] Harquail School of Earth Sciences, Laurentian University, Sudbury, Ontario P3E 2C6, Canada

ARTICLE INFO

Keywords:
Skarn deposit
Lithogeochemistry
Chemostratigraphy
Compositional data analysis
Multivariate statistics
Simplex

ABSTRACT

The Rosemont skarn deposit contains resources exceeding 1 billion tons of Cu-Mo-Ag mineralization. The deposit comprises three major structural-stratigraphic domains informally named Lower Plate, Upper Plate, and West Block. The Lower Plate is composed dominantly of Paleozoic chemical sedimentary rocks forming an east dipping homoclinal sequence. The Upper Plate overlies the Lower Plate and is composed dominantly of Mesozoic and Cenozoic siliciclastic sedimentary rocks. The West Block is dominated by Precambrian granitoids structurally interleaved with panels of Paleozoic chemical and siliciclastic sedimentary rocks. Most of the economic mineralization is hosted in the Lower Plate.

Lithological variability, structural complications of the stratigraphy, and calc-silicate metasomatism complicates the visual identification of lithologies resulting in uncertain stratigraphic domains based on drill core observations. To circumvent this problem, a deposit-scale lithogeochemical and chemostratigraphic model was developed using multivariate statistics following a compositional data analysis approach to respect the relative scale and multivariate nature of geochemical compositions. Accordingly, hierarchical cluster analysis of variables using the variation matrix as a measure of similarity, and principal component analysis on centered log-ratio coefficients (clr) were used to explore relationships between variables and to reduce dimensionality. Simplicial projections including centered tetrahedral and ternary diagrams were used to develop a lithogeochemical classification for the sedimentary rocks of the Rosemont deposit. A ternary diagram, or 3-part simplex with vertices Ca, Mg, and a composite variable given by the geometric mean of Cr, Ni, Co, V, P, Hf, Zr, Th, Ti, Al, Nb, Sc, Ta, Y, Ce, and La contains a rich data structure for lithogeochemical classification.

The lithological attributes of the Rosemont deposit can be subdivided into 7 lithogeochemical classes evident on the ternary diagram. Limestone, dolostone, and siliciclastic-crystalline classes are key end members. The remaining 4 classes represent mixed chemical-siliciclastic lithogeochemical attributes discriminating complex lithological variations induced by the incorporation of siliciclastic component in chemical sedimentary rocks. The lithogeochemical classification derived from the ternary diagram is supported by *K*-means clustering applied to two balances representing isometric logratio (ilr) coordinates of the 3-part simplex.

The geospatial distribution of the lithogeochemical classes allows the simplification of the stratigraphy of the Lower Plate into three relevant chemostratigraphic units, namely a Lower Limestone Unit and an Upper Dolostone Unit separated by a Mixed Unit of chemical-siliciclastic sedimentary rocks. It is noteworthy that ore grades are controlled by the relative proportion of chemical to siliciclastic component of the mineralized rocks. Higher metal grades are characteristic of relatively pure chemical sedimentary rocks in the Lower Limestone and Upper Dolostone Units; whereas low metal grades characterize the Mixed Unit with a large proportion of siliciclastic component. As a corollary, the lithogeochemical classification can be used as a skarn fertility tool to predict the economic potential of chemical-siliciclastic sedimentary sequences in geological environments permissive of skarn mineralization.

1. Introduction

Skarn deposits are explored and mined for their economically valuable metals including Cu, Mo, Ag, Au, W, Fe, Pb, Zn, U, REE, F, B, In, and Sn (Einaudi et al., 1981; Einaudi and Burt, 1982; Meinert, 1992; Meinert et al., 2000). Although skarn deposits have been extensively

* Corresponding author at: Hudbay, Suite 800, 25 York Street, Toronto, Ontario, Canada.
E-mail address: ordonez.jc@gmail.com (J.C. Ordóñez-Calderón).

http://dx.doi.org/10.1016/j.gexplo.2017.06.005
Received 9 April 2017; Received in revised form 28 May 2017; Accepted 8 June 2017
Available online 09 June 2017
0375-6742/

researched, most studies have traditionally aimed at understanding the petrology of skarn-related intrusions, field characteristics, tectonic setting, ore forming fluids, ore genesis, mineral chemistry, geochronology, and metasomatic evolution (Einaudi and Burt, 1982; Gaspar and Inverno, 2000; Lieben et al., 2000; Meinert et al., 2000; Deng et al., 2015; Wang et al., 2015a; Baghban et al., 2016; Li et al., 2017; Park et al., 2017; Soloviev and Kryazhev, 2017; Yang et al., 2017; Zhou et al., 2017). However, a practical problem relevant to exploration and mining is the reconstruction of the stratigraphy of skarn deposits given that intense calc-silicate metasomatism and recrystallization complicate visual discrimination of rock types. Also, lithological differences among chemical sedimentary rocks, for instance limestone versus marlstone, are subtle, which complicate the identification of lithological boundaries. These geological challenges are manifested as inconsistent lithological and stratigraphic observations within and between drill holes rendering the delineation of stratigraphic domains highly uncertain. Establishing a reliable mine-scale stratigraphy is critical for mineral resource estimation, and of economic significance for mining operations given that metallurgical parameters such as metal grades, grinding efficiency, deleterious minerals, deleterious elements, and metal recoveries are spatially related and controlled by primary lithologic and stratigraphic features (cf., Gregory et al., 2013; Lund et al., 2013; Amer et al., 2014; Pownceby and Johnson, 2014; Yildirim et al., 2014; Wang et al., 2015b; Maydagán et al., 2016; Wang et al., 2016a, 2016b).

The goal of this study was to devise a lithogeochemical and chemostratigraphic framework for the Rosemont deposit to increase the certainty of mine-scale stratigraphic domains. To achieve this goal, multivariate statistical analysis was conducted on whole-rock multielement geochemical data of approximately 33,000 samples distributed throughout the Rosemont deposit. The systematic data analysis presented in this paper follows a compositional data analysis approach to respect the multivariate relative structure of geochemical data (cf., Aitchison, 1986; Tolosana-Delgado et al., 2005; Egozcue and Pawlowsky-Glahn, 2006; van den Boogaart and Tolosana-Delgado, 2013; Barceló-Vidal and Martín-Fernández, 2016). We demonstrate that by applying mathematical transformations that are consistent with the simplicial geometry of compositional data, simple ternary diagrams can be developed for lithogeochemical classification of chemical-siliciclastic sedimentary sequences. The lithogeochemical classification is consistent within and between drill holes, which facilitates the recognition of key stratigraphic boundaries and the simplification of complex stratigraphy into relevant chemostratigraphic units that capture the most relevant lithological and geochemical variations of the Rosemont skarn deposit.

2. Geology, stratigraphy, and mineralization

The Rosemont deposit, Hudbay Minerals Inc., is a Cu-Mo-Ag skarn located in the Laramide porphyry belt of Arizona, 40 km to the southeast of Tucson. The deposit contains over 1 billion tons of mineralized rocks hosted dominantly within a Paleozoic chemical sedimentary sequence (Fig. 1). Three major structural-stratigraphic domains characterize the deposit, namely (1) the Lower Plate, (2) the Upper Plate, and (3) the West Block (Figs. 2–3).

The Lower Plate forms an upright, east-dipping, homoclinal sequence composed dominantly of Paleozoic chemical sedimentary rocks with minor interbedded siliciclastic rocks. Several Paleozoic formations form the Lower Plate of the Rosemont skarn deposit. From bottom to top, these are the Mississippian to Permian Escabrosa, Horquilla, Earp, Colina, Epitaph, and Scherrer Formations (Fig. 3) (cf., Johnson and Ferguson, 2007; Ferguson, 2009; Ferguson et al., 2009; Rasmussen et al., 2012).

The Escabrosa and Horquilla Formations comprise dominantly thickly-bedded limestone (Fig. 4A–B). However, marlstone, calcareous siltstone, mudstone, and siltstone become more abundant towards the upper parts of the Horquilla Formation (Rasmussen et al., 2012; this study). The Earp Formation is a mixed chemical-siliciclastic sedimentary sequence composed of bedded marlstone, calcareous sandstone, calcareous siltstone, fine-grained sandstone, siltstone, and mudstone (Fig. 4C). The Colina and Epitaph Formations, called the Epitaph Group in the Rosemont deposit, comprise dominantly dolostone and limestone (Fig. 4D). The occurrence of the Scherrer Formation in the Lower Plate is controversial given the paucity of drill holes higher up in the stratigraphy and outside of the economic ore body. The Scherrer Formation is composed of interbedded siltstone, calcareous siltstone, calcareous sandstone, dolostone, and limestone.

The Upper Plate is composed dominantly of Mesozoic and Cenozoic siliciclastic and volcanic rocks overlying the Lower Plate (cf., Johnson and Ferguson, 2007; Ferguson, 2009; Ferguson et al., 2009; Rasmussen et al., 2012; this study). A low angle fault, an unconformity that has been structurally overprinted, bounds the Lower and Upper Plates (Fig. 2). The Upper Plate includes the Jurassic-Cretaceous Glance Formation, and the Cretaceous Willow Canyon Formation (Fig. 3) (Drewes, 1971; Johnson and Ferguson, 2007; Ferguson, 2009; Ferguson et al., 2009; Rasmussen et al., 2012). The Glance Formation is a thickly-bedded, clast-supported, polymictic conglomerate with abundant limestone clasts and carbonate-rich matrix. In the Rosemont deposit the limestone conglomerate and some structural panels of limestone and minor dolostone, inferred to represent the Permian Concha and Rain Valley Formations, are informally called the Glance Group (Figs. 2–3). The Willow Canyon Formation is a succession of cross-stratified arkose, silty sandstone, and mudstone. A stratigraphic marker within the Willow Canyon Formation is a volcanic unit comprising lava flows and volcaniclastic rocks of andesitic composition (Figs. 2–3). The siliciclastic sedimentary rocks of the Willow Canyon Formation and the andesitic volcanic rocks are informally named the Arkose Group in the Rosemont deposit.

The most distinctive Cenozoic unit in the Upper Plate is the Pliocene-Miocene Gila Conglomerate (Drewes, 1972a, 1972b; Johnson and Ferguson, 2007; Ferguson, 2009; Ferguson et al., 2009; Rasmussen et al., 2012; this study). This unconsolidated conglomerate is polymictic with clasts ranging from granitoid, arkose, andesite, and minor limestone deposited within a normal-fault-bounded basin.

The West Block is bounded to the Lower Plate by the steeply-dipping backbone fault system (Fig. 2). The dominant lithological unit of the West Block is the Precambrian Granitoids (Johnson and Ferguson, 2007; Ferguson, 2009; Ferguson et al., 2009; Rasmussen et al., 2012). However, the contact with the Lower Plate comprises structurally interleaved panels of the Precambrian Granitoids, and sedimentary formations including the Cambrian Bolsa Quartzite and Abrigo Formations, and the Devonian Martin Formation (Figs. 2–3). The Bolsa Quartzite Formation is distinctively composed of coarse-grained quartz sandstone. The Abrigo Formation consists dominantly of interbedded limestone, fine-grained sandstone, siltstone, and mudstone, whereas the Martin Formation is dominated by dolostone.

Tertiary quartz-feldspar porphyries intrude the Lower Plate below the low angle fault (cf., Keith and Wilt, 1986). These porphyritic intrusions are economically mineralized with Cu, Mo, and Ag and are thought to be the source of mineralization and calc-silicate metasomatism of the Rosemont skarn deposit (Figs. 1 and 3).

Calc-silicate alteration in the Lower Plate and chemical sedimentary rocks of the West Block are characterized by fine to very fine-grained skarn facies such as garnet, pyroxene, wollastonite, and serpentine skarn. In contrast, metasomatism in the Upper Plate is dominated by massive fine-grained epidote alteration.

Most of the economic mineralization is hosted in the Lower Plate (Fig. 2). The highest Cu grades are hosted in the upper part of Escabrosa, Horquilla, and Epitaph Group; whereas lower metal grades are typical of the Earp Formation. Some low-grade economic mineralization is hosted in the Upper Plate Arkose Group (Figs. 2–3). The West Block contains some economic mineralization, mostly hosted in structurally interleaved chemical sedimentary rocks of the Abrigo and

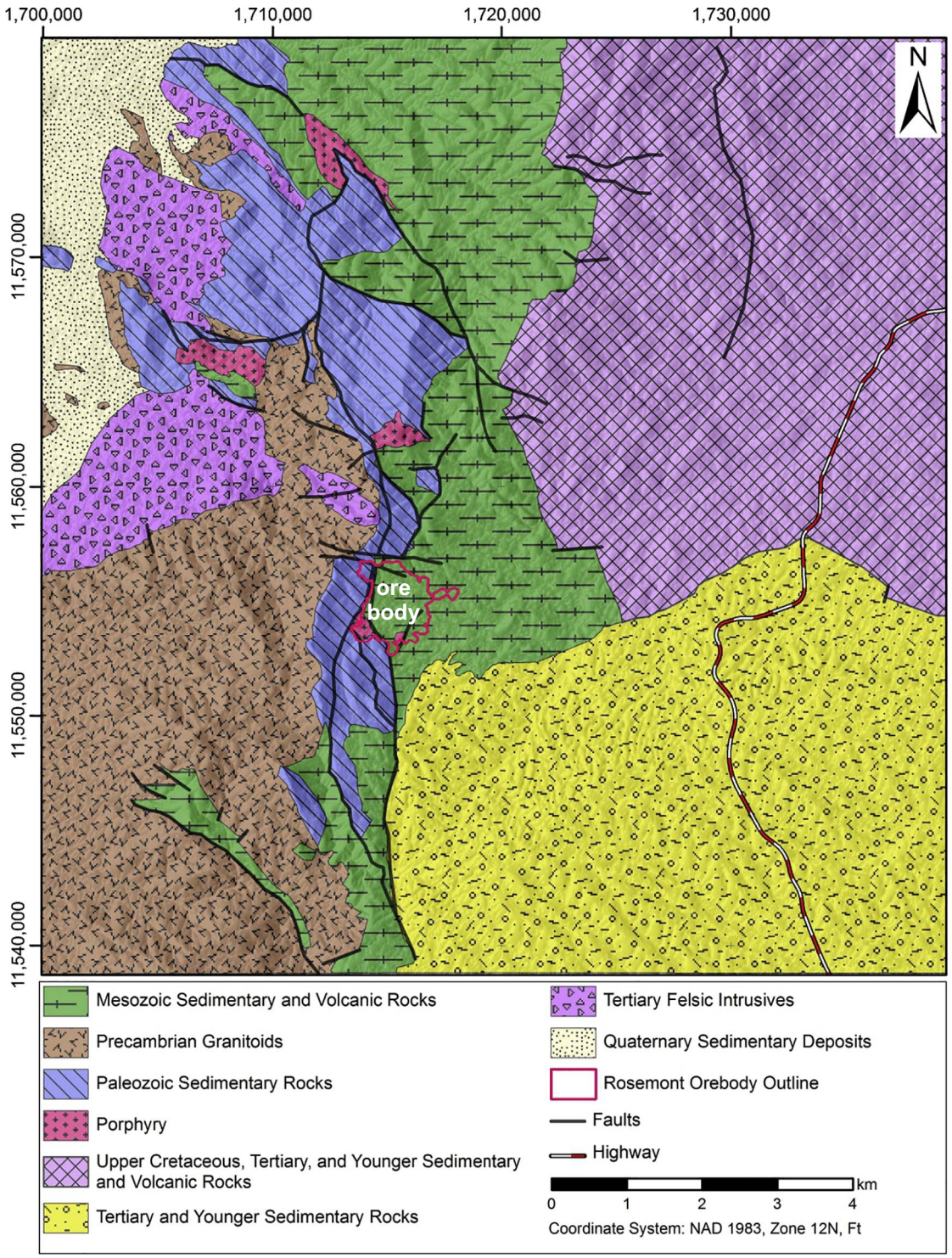

Fig. 1. Regional geological map of the Rosemont area with projection of the Cu, Mo, and Ag skarn mineralization (After Ferguson, 2009 and Ferguson et al., 2009). The mineralization is not exposed and is dominantly hosted within a Paleozoic chemical sedimentary sequence (Lower Plate) overlaid by a sequence of Mesozoic and Cenozoic siliciclastic sedimentary rocks (Upper Plate).

Martin Formation.

3. Methods and terminology

3.1. Sampling and whole rock geochemistry

In this study, drill core samples with multi-element geochemical data are referred as observations, compositions, or compositional vectors, whereas chemical elements are referred as variables, parts, or components.

The whole rock multi-element geochemical dataset of the Rosemont deposit comprises 33,000 drill core samples homogeneously distributed throughout the deposit. These samples were collected from 90 diamond drill holes sampled at 1.5 m intervals along the entire core length to properly characterize the lithological variability of the deposit. All samples were analyzed at Bureau Veritas laboratories in Vancouver, Canada, for 45 elements by inductively coupled plasma mass spectrometry after a 4-acid digestion (Bureau Veritas method MA200).

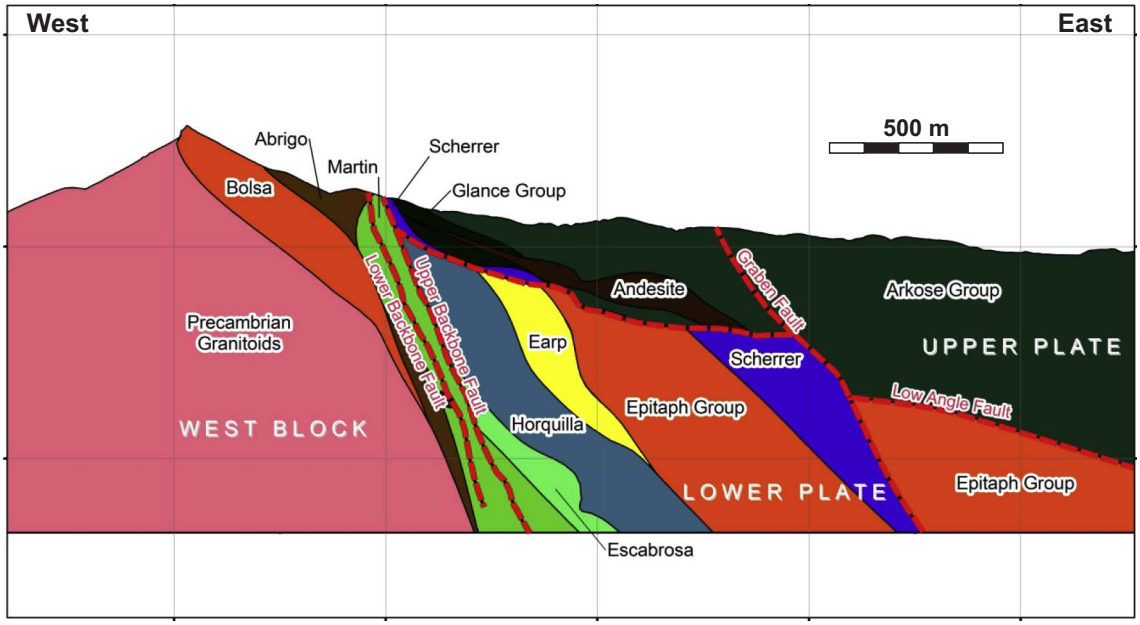

Fig. 2. Geological cross section illustrating the structural and stratigraphic domains of the Rosemont deposit. The cross section was reconstructed using core logging and the lithogeochemical model discussed in this study.

Era	Period	Formation	Formation Simplified	Thickness (m)	Section
Cenozoic	Tertiary	Porphyry			
Mesozoic	Cretaceous	Willow Canyon	Arkose Group	700	Andesite
	Jurassic	Glance	Glance Group	0-500	
Paleozoic	Permian	Rain Valley	Glance Group	0-100	
		Concha		100-200	
		Scherrer		200	
		Epitaph	Epitaph Group	300	
		Colina		100	
		Earp		250	
	Pennsylvanian	Horquilla		300	
	Mississippian	Escabrosa		200	
	Devonian	Martin		120	
	Cambrian	Abrigo		200-300	
		Bolsa Quartzite		150	
Precambrian	Undifferentiated Proterozoic	Granitoids			

Fig. 3. Schematic stratigraphy of the Rosemont area after Drewes (1972b). For simplicity some stratigraphic units were grouped together (Formation Simplified).

Variables with > 50% observations below the lower detection limit were removed from the dataset. Given that the aim of this study is to develop a lithogeochemical and chemostratigraphic model for the Rosemont deposit, a subcomposition of 18 elements was selected to include only those elements that are immobile during metasomatic alteration and contain information on rock-forming processes (Table 1). Accordingly, immobile elements used to track provenance of siliciclastic sediments and magmatic fractionation processes include the major elements Al and P, the high field strength elements (HFSE) Hf, Zr, Th, Ti, Nb, Ta, and Y, the light rare earth elements (LREE) La and Ce, and the transition metals (TM) Sc, Cr, Ni, Co, and V (Taylor and McLennan, 1985; Bhatia and Crook, 1986; MacLean and Barrett, 1993; McLennan, 2001; Kelemen et al., 2003; Kemp and Hawkesworth, 2003; Rudnick and Gao, 2003; Caja et al., 2007; Ordóñez-Calderón et al., 2008, 2016; Mungal, 2014; Plank, 2014). Although Ca and Mg are mobile during metasomatic alteration, these two major elements were included in the 18-part subcomposition given that they are the most important components of limestone and dolostone (Table 1). Other mobile elements including major elements (Na, K, Fe, and Mn), various trace elements (Ba, Be, Li, Pb, Rb, Sr, and U), and ore-related target and pathfinder metals (Cu, Mo, Ag, Zn, As, Bi, Cd, In, Re, S, Sb, Se, Sn, Te, Tl, and W) were not used in this study for lithogeochemical modelling.

The quality of the geochemical data was evaluated using certified reference materials (CRMs) OREAS 501b, 502b, 503b, 504b, 902, and 930, which are certified for up to 55 major and trace elements. Table 1 summarizes the analytical results for three selected CRMs. The precision is expressed as the percent relative standard deviation (RSD%) of the CRM values. The accuracy is reported as bias, which is calculated as the percent difference between the average CRM value obtained from the laboratory measurements and the best value recommended by the CRM certificate (Table 1).

The CRM analysis indicates precisions better than 10% for most major and trace elements, and 10 to 15% for La, Ce, and Th (Table 1). The bias is better than ± 10% for most analytes, and 10 to 18% for La, Ce, and Th. In addition, the results from coarse and fine blanks OREAS 26a and 22d indicate no significant contamination with elements of interest in this study. Accordingly, the multi-element geochemical dataset is deemed of good quality for lithogeochemical modelling.

3.2. Data analytics strategy

3.2.1. Data imputation

Left-censored and right-censored data are, respectively, nondetects below and above the laboratory reporting limits (Sinha et al., 2006; Helsel, 2012). The 18-part subcomposition used in this study contains only left-censored values. Censored data complicates multivariate statistical analysis given that methods such as cluster analysis and

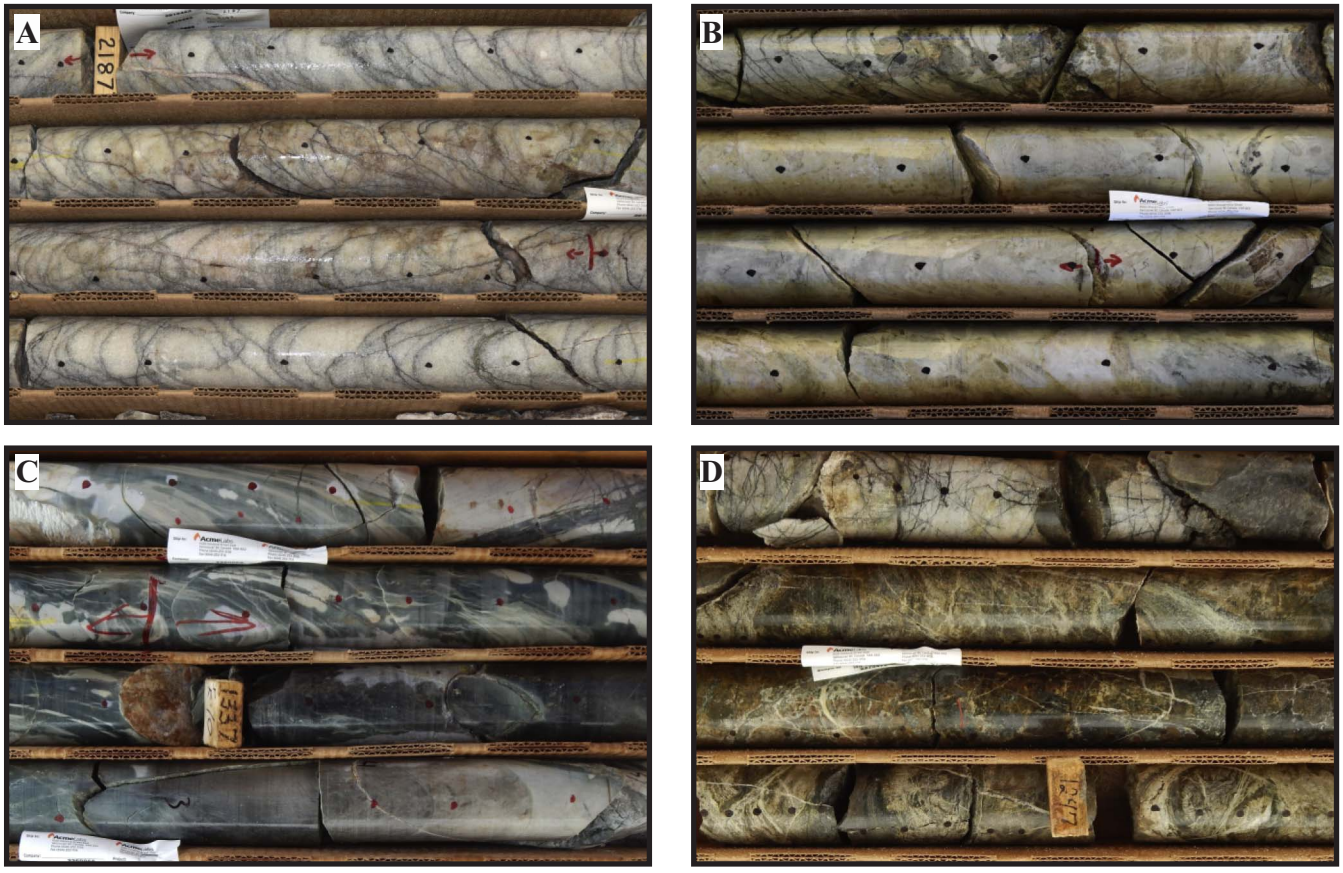

Fig. 4. Diamond drill core photographs of selected lithologies of the Rosemont deposit. (A) Pure and (B) impure limestones belonging, respectively, to the lithogeochemical classes limestone and siliciclastic-limestone (Section 4.2.2, Fig. 9). (C) Intercalation of well bedded calcareous siltstone belonging to the lithogeochemical class siliciclastic-dolostone (Section 4.2.2, Fig. 9). (D) Dolostone belonging to the dolostone class (Section 4.2.2, Fig. 9).

Table 1
Analytical data for selected certified reference materials (CRMs) analyzed in this study. Precision is expressed as percent relative standard deviation (RSD%). Bias is calculated as the percent difference between the average value and the best value (BV) recommended in the CRM certificate. The lower detection limits (LDL) are reported for the analytes discussed in this study.

Variable	Unit	LDL	OREAS 501b (N = 385)					OREAS 502b (N = 378)					OREAS 503b (N = 370)				
			BV	Average	SD	RSD(%)	Bias(%)	BV	Average	SD	RSD(%)	Bias(%)	BV	Average	SD	RSD(%)	Bias(%)
Al	%	0.01	7.68	7.14	0.41	6%	− 7%	7.47	7.10	0.35	5%	− 5%	7.45	7.04	0.42	6%	− 5%
Ca	%	0.01	2.71	2.68	0.09	3%	− 1%	2.71	2.68	0.09	4%	− 1%	2.73	2.69	0.11	4%	− 1%
Ce	ppm	1	68	57.40	6.96	12%	− 16%	61	53.90	5.86	11%	− 12%	59.00	53.98	5.83	11%	− 9%
Co	ppm	0.2	15.8	17.02	0.86	5%	+ 8%	20.2	21.39	1.01	5%	+ 6%	17.10	18.17	0.87	5%	+ 6%
Cr	ppm	1	86	85.60	4.99	6%	− 0.5%	84	83.68	4.75	6%	− 0.4%	84.00	83.23	4.94	6%	− 1%
Hf	ppm	0.1	2.54	2.38	0.16	7%	− 6%	2.27	2.18	0.15	7%	− 4%	2.25	2.20	0.16	7%	− 2%
La	ppm	0.1	33	27.18	4.03	15%	− 18%	29.9	25.87	3.47	13%	− 13%	30.00	26.12	3.40	13%	− 13%
Mg	%	0.01	1.48	1.46	0.05	4%	− 2%	1.54	1.52	0.05	3%	− 1%	1.54	1.52	0.05	3%	− 1%
Nb	ppm	0.1	18	17.63	0.75	4%	− 2%	16.2	15.8	0.67	4%	− 2%	16.00	15.59	0.93	6%	− 3%
Ni	ppm	0.1	41.5	45.44	2.57	6%	+ 9%	37.2	40.65	2.31	6%	+ 9%	38.70	41.84	2.23	5%	+ 8%
P	%	0.001	0.102	0.103	0.005	5%	+ 1%	0.100	0.101	0.01	6%	+ 1%	0.10	0.10	0.01	5%	+ 1%
Sc	ppm	1	12.90	12.19	0.77	6%	− 5%	13.2	12.89	0.75	6%	− 2%	13.10	12.77	0.76	6%	− 3%
Ta	ppm	0.1	1.38	1.29	0.07	5%	− 7%	1.17	1.14	0.06	6%	− 3%	1	1.13	0.06	6%	− 6%
Th	ppm	0.1	18	15.82	2.10	13%	− 12%	15.8	14.27	1.65	12%	− 10%	15.60	14	1.60	11%	− 7%
Ti	%	0.001	0.466	0.49	0.01	3%	+ 4%	0.44	0.47	0.02	4%	+ 6%	0.44	0.47	0	4%	+ 6%
V	ppm	1	121	127.79	5.69	4%	+ 6%	126	134.12	6.03	4%	+ 6%	127.00	135.35	6.42	5%	+ 7%
Y	ppm	0.1	24.6	22.48	2.05	9%	− 9%	23.3	21.57	1.83	9%	− 7%	22.90	21.40	1.66	8%	− 7%
Zr	ppm	0.1	77	74.39	3.69	5%	− 3%	71	68.58	3.59	5%	− 3%	71.00	68.86	4.21	6%	− 3%

principal component analysis require complete data matrices. In geochemistry, a typical approach is to replace left-censored values with a fixed fraction, commonly half the lower detection limit. However, this approach may change the relative variation structure between components, which is critical in multivariate data analysis (Martín-Fernández et al., 2003; Palarea-Albaladejo et al., 2014; Palarea-Albaladejo and Martín-Fernández, 2013, 2015).

Accordingly, nondetects were imputed, prior to any mathematical transformation of variables for statistical analysis, using the robust multiplicative lognormal replacement method, which is part of the R package 'zCompositions' (Palarea-Albaladejo et al., 2014; Palarea-Albaladejo and Martín-Fernández, 2015). This method is sensible for

this study because it respects the compositional nature of the data, is computationally feasible for large datasets, can be applied to data matrices in which all observations contain one or more variables with left-censored values, does not assume multivariate normality, and it is appropriate for positive data with right-skewed distributions typical of geochemical variables (Martín-Fernández et al., 2003; Helsel, 2012; Palarea-Albaladejo et al., 2014; Palarea-Albaladejo and Martín-Fernández, 2013, 2015).

3.2.2. Compositional data analysis

Compositional data, or compositions, are vectors of positive components in which the relevant information is assumed to be contained only in the ratio between the parts (Aitchison, 1986; Egozcue and Pawlowsky-Glahn, 2006; Pawlowsky-Glahn and Egozcue, 2006; Barceló-Vidal and Martín-Fernández, 2016). These vectors have special mathematical properties that preclude the direct application of multivariate statistical techniques to raw compositional data because these techniques are designed for unconstrained real spaces in which variables are free to vary from -∞ to + ∞. These assumptions are not met by compositional vectors, which are strictly positive and define a constrained space imposed by the constant sum of the components.

A *D*-part composition can be subdivided into a subcomposition by taking two or more components and performing a closure operation such that its parts sum to a positive constant, for instance 1 for proportions, and 100 for percentages. The key point for creating subcompositions is to reduce dimensionality and to focus the analysis on the information contained in the ratios between the parts that are of interest to the analyst. In this study, all mathematical transformations and statistical analysis were performed on the 18-part subcomposition described on Section 3.1.

Compositions can be represented in the *D*-part simplex $\mathbb{S}^D$ by closing them to a constant. A simplex is the generalization of the mathematical properties of an equilateral triangle or ternary diagram, a 3-part simplex, into the *D*-part simplex or hypertetrahedron. The simplex can be equipped with an alternative geometry, which has been shown to be appropriate and relevant for geochemical data because it represents the data in its relative scale. This simplicial geometry is based on ratios between elements, which are the quantities capturing relative information (Aitchison, 1986; Martín-Fernández et al., 1998; Barceló-Vidal et al., 2001; Pawlowsky-Glahn and Egozcue, 2001; Miller, 2002; von Eynatten et al., 2002; Mateu-Figueras, 2003; Aitchison and Egozcue, 2005; Tolosana-Delgado et al., 2005; Egozcue and Pawlowsky-Glahn, 2006; Pawlowsky-Glahn and Egozcue, 2006; Pawlowsky-Glahn et al., 2015; Barceló-Vidal and Martín-Fernández, 2016).

In geochemical analysis it is often desired to group several chemical elements into a single composite variable to investigate specific geological processes and for graphic representations such as ternary diagrams. Traditionally, ternary diagrams use amalgamation, summation of parts, to group variables and reduce dimensionality (Irving and Baragar, 1971; Pearce and Cann, 1973; Wood, 1980; Mullen, 1983; Nesbitt and Young, 1984, 1989; Bhatia and Crook, 1986; Harris et al., 1986; Meschede, 1986; Fedo et al., 1995; Ohta and Arai, 2007). It is noteworthy that amalgamation is not consistent with the mathematical principles of compositional data analysis because the transformed data do not preserve the geometric relationships (Egozcue and Pawlowsky-Glahn, 2005). In this contribution, composite variables, or composite parts, were calculated using the geometric mean of the group expressed as:

$$g = (x_1 x_2 ... x_D)^{1/D} \tag{1}$$

The geometric mean produces a new component behaving mathematically consistent with simplicial geometry (Aitchison et al., 2002; Egozcue and Pawlowsky-Glahn, 2006; Pawlowsky-Glahn and Egozcue, 2006; van den Boogaart and Tolosana-Delgado, 2013).

In addition, most traditional ternary diagrams use multiplication by arbitrary scalars to re-scale one or more variables when the parts have different magnitudes (e.g., major versus trace elements) to prevent the data cloud from collapsing on the vertex or border of the variables with larger magnitude. To avoid subjective re-scaling, we performed centering operations around the center of the compositional data matrix $\mathbf{X} = [X_1, X_2, \ldots, X_D]$, which is given by:

$$cen(\boldsymbol{X}) = C\,[g(X_1), g(X_2), ..., g(X_D)] \tag{2}$$

where *C* denotes the closure operation (Martín-Fernández et al., 1998; von Eynatten et al., 2002; Egozcue and Pawlowsky-Glahn, 2006; Pawlowsky-Glahn and Egozcue, 2006; Pawlowsky-Glahn et al., 2015; van den Boogaart and Tolosana-Delgado, 2013). The centered dataset is obtained by perturbing the compositional vectors by the inverse of the center (Eq. (2)) and reclosing them to a constant:

$$\boldsymbol{x}_i = C\,[x_{i1}/g(X_1), x_{i2}/g(X_2), ..., x_{iD}/g(X_D)] \tag{3}$$

The centering operation described above is compatible with simplicial geometry (*op. cit.*).

Compositional vectors in $\mathbb{S}^D$ can be transformed into coordinates belonging to the Euclidean vector space in $\mathbb{R}^{D-1}$, which can be used with any multivariate statistical technique without the problems of closure and constrained spaces typical of raw compositional data. In this contribution, coordinates were calculated using the isometric log-ratio (ilr) transformation (Egozcue et al., 2003; Egozcue and Pawlowsky-Glahn, 2006).

To facilitate interpretation of the ilr-coordinates the concept of balances between groups of parts was applied (Egozcue and Pawlowsky-Glahn, 2005; Egozcue and Pawlowsky-Glahn, 2006; Buccianti et al., 2016). Balances are calculated using a sequential binary partition in which the *D*-parts are systematically divided into two non-overlapping composite variables following (*D*-1) steps. The procedure results in (*D*-1) ilr-variables, or coordinates, representing balances between groups in $\mathbb{R}^{D-1}$. The coordinates are given by:

$$ilr_i = \sqrt{rs/(r+s)}\,\ln(g(c_+)/g(c_-)) \tag{4}$$

where $i = \{1, 2, \ldots, (D-1)\}$, the log-ratio represents the natural logarithm taken to the quotient of the geometric mean of the *r* variables in the numerator $g(c_+)$ divided by the geometric mean of the *s* variables in the denominator $g(c_-)$.

An additional representation of compositional data used in this study is the centered log-ratio transformation (clr) (Aitchison, 1986). The clr coefficient of a compositional vector $\mathbf{x}$ in $\mathbb{S}^D$ is obtained by dividing each component by the geometric mean of the composition and then taking the natural logarithm

$$\mathrm{clr}(\boldsymbol{x}) = [ln(x_1/g(\boldsymbol{x})), ln(x_2/g(\boldsymbol{x})), ..., ln(x_D/g(\boldsymbol{x}))] \tag{5}$$

In this study, the correlation and covariance matrices of the raw geochemical data were avoided because of the spurious effects of closure (Pearson, 1897; Chayes, 1960, 1971, 1975; Aitchison, 1986). To circumvent these problems, the codependence between all possible pairwise variables was evaluated using the variation matrix (Aitchison, 1986) defined by the equation

$$\tau_{ij} = \mathrm{var}(\ln(x_i/x_j)) \tag{6}$$

The variation matrix explains how the total dispersion of a compositional dataset is distributed among all possible log-ratios. The τ_{ij} values represent the regular variance (var) of the associated logratios. A low τ_{ij} value is indicative of small variance of the associated logratio indicating good proportionality between the components.

In this study, all the compositional data analysis and associated calculations were conducted using the R package 'compositions' (van den Boogaart and Tolosana-Delgado, 2013; van den Boogaart et al., 2015).

3.2.3. Multivariate statistical methods

Exploring a multi-element geochemical dataset in order to find

Table 2
Variation Matrix. Bold font numbers indicate the strongest colum-wise codependence.

Variable	Al	Ca	Ce	Co	Cr	Hf	La	Mg	Nb	Ni	P	Sc	Ta	Th	Ti	V	Y	Zr
Al	0	5.78	0.23	0.93	1.54	0.71	0.43	2.92	**0.13**	1.58	1.24	0.38	0.35	**0.26**	0.22	0.84	0.73	0.82
Ca	5.78	0	4.82	4.16	2.26	3.73	4.02	2.01	5.09	2.40	3.65	4.34	4.37	5.75	5.54	3.68	3.17	3.80
Ce	0.23	4.82	0	0.70	1.15	0.61	**0.10**	2.43	0.18	1.22	1.00	0.31	0.30	0.29	0.32	0.61	0.41	0.73
Co	0.93	4.16	0.70	0	1.01	0.77	0.74	1.95	0.69	1.02	1.16	0.68	0.84	1.22	0.79	**0.44**	0.81	0.83
Cr	1.54	2.26	1.15	1.01	0	0.99	0.85	1.26	1.21	**0.26**	0.87	0.88	1.00	1.73	1.35	0.68	0.62	1.06
Hf	0.71	3.73	0.61	0.77	0.99	0	0.61	1.82	0.50	1.06	1.16	0.65	0.59	0.87	0.69	0.78	0.66	**0.12**
La	0.43	4.02	**0.10**	0.74	0.85	0.61	0	2.16	0.34	0.96	0.75	0.29	0.29	0.48	0.53	0.51	**0.21**	0.77
Mg	2.92	**2.01**	2.43	1.95	1.26	1.82	2.16	0	2.50	1.23	2.25	2.32	2.30	2.92	2.70	2.02	1.90	1.74
Nb	**0.13**	5.09	0.18	0.69	1.21	0.50	0.34	2.50	0	1.26	1.11	0.30	0.23	0.31	**0.17**	0.65	0.53	0.62
Ni	1.58	2.40	1.22	1.02	**0.26**	1.06	0.96	**1.23**	1.26	0	1.00	0.93	1.13	1.82	1.31	0.84	0.73	1.10
P	1.24	3.65	1.00	1.16	0.87	1.16	0.75	2.25	1.11	1.00	0	0.84	0.93	1.52	1.23	0.72	0.70	1.31
Sc	0.38	4.34	0.31	0.68	0.88	0.65	0.29	2.32	0.30	0.93	0.84	0	**0.17**	0.64	0.34	0.46	0.34	0.90
Ta	0.35	4.37	0.30	0.84	1.00	0.59	0.29	2.30	0.23	1.13	0.93	**0.17**	0	0.51	0.46	0.64	0.36	0.86
Th	0.26	5.75	0.29	1.22	1.73	0.87	0.48	2.92	0.31	1.82	1.52	0.64	0.51	0	0.47	1.13	0.77	0.99
Ti	0.22	5.54	0.32	0.79	1.35	0.69	0.53	2.70	0.17	1.31	1.23	0.34	0.46	0.47	0	0.74	0.74	0.77
V	0.84	3.68	0.61	**0.44**	0.68	0.78	0.51	2.02	0.65	0.84	0.72	0.46	0.64	1.13	0.74	0	0.53	0.87
Y	0.73	3.17	0.41	0.81	0.62	0.66	0.21	1.90	0.53	0.73	**0.70**	0.34	0.36	0.77	0.74	0.53	0	0.87
Zr	0.82	3.80	0.73	0.83	1.06	**0.12**	0.77	1.74	0.62	1.10	1.31	0.90	0.86	0.99	0.77	0.87	0.87	0

relationships between variables and to generate subcompositions to map geological processes can be a challenging and time consuming task. For instance, $D(D\text{-}1)/2$ scatterplots or Harker diagrams, D representing the number of variables, are needed to fully investigate relationships between different variables. A total of 990 scatterplots would be needed to visualize a typical 45 element geochemical dataset. This approach is inefficient and for compositional data the closure problem may induce negative correlations and misrepresentations in scatterplots (Pearson, 1897; Chayes, 1960, 1971, 1975; Aitchison, 1986). To circumvent these problems, the variation matrix (Eq. (6), Section 3.2.2) was used as a measure of similarity in hierarchical cluster analysis in order to cluster variables instead of observations (Aitchison, 1986; van den Boogaart and Tolosana-Delgado, 2013; Pawlowsky-Glahn et al., 2015). For instance, a value of 0 in the variation matrix indicates perfect association, whereas large values indicate strong independence between variables (Aitchison, 1986; van den Boogaart and Tolosana-Delgado, 2013; Pawlowsky-Glahn et al., 2015). The results of hierarchical clustering can be graphically displayed and easily interpreted in a cluster dendrogram, a decision tree-like diagram of all possible clusters representing the hierarchical agglomeration of the data structure. Grouping variables based on a cluster dendrogram facilitates identification of variables that are codependent and carry similar information.

K-means cluster analysis was used to cluster observations based on a set of variables. This technique seeks to find non-overlapping groups in a dataset by partitioning the sample space into K pre-specified number of clusters (MacQueen, 1967). The technique finds groups with the smallest possible within-cluster variation, which is achieved by minimizing the average pairwise squared Euclidean distance within the k-th cluster (Hartigan and Wong, 1979). In this study, *K*-means clustering was applied to ilr-transformed variables (Eq. (4)) because the closure of raw compositional data deforms Euclidean distances, which may result in misleading interpretations.

In *K*-means clustering the decision of the optimum number of clusters is not trivial. A statistical solution is to perform several *K*-means cluster analysis with different choices of K to calculate the total within-cluster sum of square errors for each K. The optimum number of clusters is then decided based on the location of an inflection on plots of total within-cluster sum of square errors against the number of K-clusters. However, more often the decision of the optimum number of K-clusters requires domain-specific knowledge.

Principal component analysis (PCA) is commonly used in exploratory data analysis to reveal hidden structure in a dataset and to identify associations among variables that can be used to explain geological and geochemical processes (e.g., Davies, 2002; Grunsky, 2010; van den Boogaart and Tolosana-Delgado, 2013). The technique aims to explain the variation within a dataset by reducing its dimensionality in order to filter noise and reduce redundancy among correlated variables (Davies, 2002; Jolliffe, 2002; Husson et al., 2011). Performing PCA on a dataset returns transformed observations commonly referred to as principal component scores (e.g., PC1, PC2, etc.), and vectors of coefficients known as loadings, which represent projections of the principal components onto the original variables. Principal components scores and loadings can be simultaneously visualized using a biplot to acquire insight regarding data structure and related groups of variables (Gabriel, 1971; Gower and Hand, 1996; Aitchison and Greenacre, 2002; Gower et al., 2011). In this study, PCA was done by singular value decomposition on clr coefficients (Eq. (5)) after centering the dataset as explained on Section 3.2.2 (Eqs. (2) and (3)) (van den Boogaart and Tolosana-Delgado, 2013).

The multivariate statistical analysis presented in this contribution was performed using the standard statistical libraries of the R language for statistical computing (R Core Team, 2017).

3.3. Geospatial 3D–modelling

Spatial modelling of categorical variables such as lithogeochemical classes was performed using the standard implicit 3D–modelling tools of Leapfrog Geo®. Simplified categorical variables representing chemostratigraphic units were built after compositing lithogeochemical classes at 5 m intervals to smooth contacts (Section 4.3). The new composite intervals contain a large density of contact points among chemostratigraphic units throughout the deposit, which allowed the delineation of unbiased reference surfaces to create a 3D–geological model of the Rosemont deposit.

4. Results and discussion

4.1. Exploratory data analysis

4.1.1. Hierarchical cluster analysis on compositional variables

Table 2 displays the variation matrix for an 18-part subcomposition from the Rosemont deposit. The variation matrix shows clearly the geochemical affinity between different groups of elements (Table 2). Small τ_{ij} values indicate high codependence, or similarity, between components. Accordingly, Ca has the strongest codependence with Mg ($\tau_{CaMg} = 2.01$), followed by Cr ($\tau_{CaCr} = 2.26$), and other TM. In contrast, Mg shows a stronger codependence with Ni ($\tau_{MgNi} = 1.23$), followed by TM and HFSE ($\tau_{MgCr} = 1.26, \tau_{MgZr} = 1.74$). Lanthanum shows a strong relationship with Ce ($\tau_{LaCe} = 0.1$), HFSE ($\tau_{LaY} = 0.21, \tau_{LaTa} = 0.29$), and

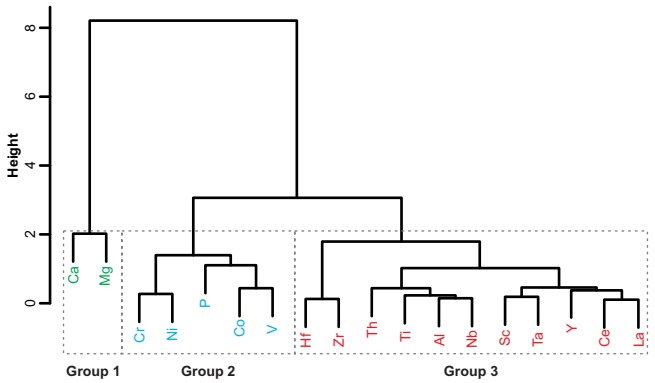

Fig. 5. Cluster dendrogram derived from hierarchical cluster analysis of a subcomposition with 18 variables using the variation matrix as a measure of similarity. Groups 1, 2, and 3 represent the clustered variables discussed in this study.

Sc ($\tau_{LaSc} = 0.29$) (Table 2).

The elemental associations represented by the variation matrix clearly reflect complex rock-forming processes that have operated at the Rosemont deposit (Table 2). For instance, the association between Ca and Mg reflects dolomitization of chemical sedimentary rocks. In contrast the strong association of TM, HFSE, and LREE reflects the interplay of mafic and felsic sources in the provenance of the siliciclastic sediments, and fractionation processes in the magmatic rocks.

Fig. 5 presents a cluster dendrogram derived from hierarchical cluster analysis applied to the variation matrix of the 18-part subcomposition. The vertical axis of dendrogram is a measure of similarity related to the variation matrix. As we move up in the dendrogram, leaves fuse into group of variables indicating similarity. Fusions occurring in the lower part of the dendrogram correspond to groups of variables that are more similar to each other, relative to those groups fused higher up in the tree (Fig. 5). At least three major groups of variables are recognized in the cluster dendrogram. Group 1 includes Ca and Mg, Group 2 is composed of Cr, Ni, Co, V, and P, and Group 3 is composed of Hf, Zr, Th, Ti, Nb, Ta, Y, La, Ce, Sc, and Al (Fig. 5).

Group 1 represents the geochemical characteristics of limestone and dolostone. Groups 2 and 3 represent the dominant geochemical attributes of siliciclastic sedimentary rocks and crystalline rocks, mostly volcanic and intrusive rocks (Fig. 5). Variations in Groups 2 and 3 variables can be attributed to provenance in siliciclastic rocks and different degrees of fractionation in crystalline rocks.

The association of variables revealed by the cluster dendrogram suggests that the 18-part subcomposition contains sufficient information to investigate the lithological attributes of the Rosemont deposit.

4.1.2. Compositional principal component analysis

Principal component analysis was performed to explore relationships between groups of variables in the 18-part subcomposition and for comparison with the cluster dendrogram (Fig. 5). This subcomposition consists primarily of immobile elements and therefore it is expected that PCA will capture lithological variability independent of metasomatic alteration and mineralization.

The quality of the information contained in the PCs is visualized on a screen plot representing the proportion of variance explained by the different principal components (Fig. 6A). Approximately 66% of the total variance is explained by PC1 and PC2, and 80% of the total variance is explained by the first four principal components (Fig. 6A).

Fig. 6B shows the covariance biplot for the PCA. It is noteworthy that the principal component loadings show groups of variables that are comparable to those suggested by the cluster dendrogram derived from hierarchical cluster analysis using the variation matrix (Fig. 5). These similarities are expected since the links joining the arrow heads of the PC loadings represent the logratios between the variables and therefore the proximity among group of variables is related to the variation

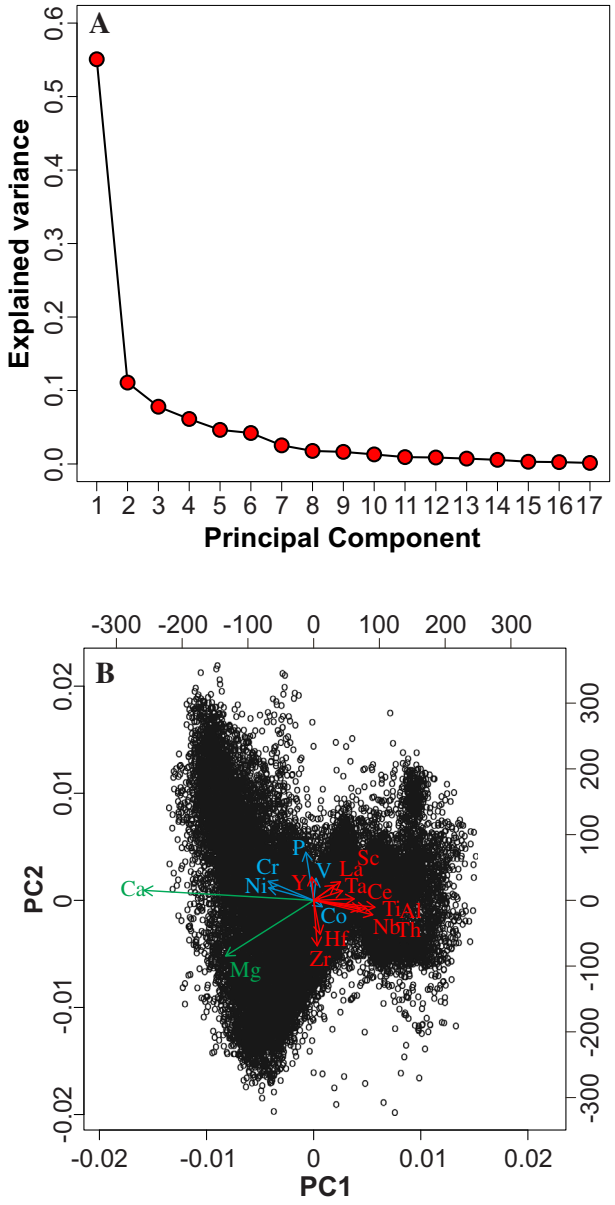

Fig. 6. Results from compositional principal component analysis. (A) Scree plot illustrating the proportion of variance explained by the principal components (PC). The PC1 and PC2 explain 66% of the total variance contained in the 18-part subcomposition of the Rosemont geochemical dataset. (B) Principal component covariance biplot. The principal component loadings are color coded to facilitate comparison with the cluster dendrogram on Fig. 5. The principal component scores (circles) reveal a data structure with at least 2 major clusters well separated by the PC1. Clusters with positive PC1 scores represent siliciclastic and crystalline rocks, whereas those with negative PC1 scores represent chemical sedimentary rocks of the Rosemont deposit.

matrix (van den Boogaart and Tolosana-Delgado, 2013).

The PC scores show a rich data structure with two dominant clusters separated by the PC1 and geochemically controlled by Group 1 (Ca and Mg) and Group 3 (HFSE, LREE, and Sc) variables (Fig. 6B). Observations with positive PC1 scores represent Rosemont siliciclastic sedimentary rocks and crystalline rocks, whereas those with negative PC1 scores represent Rosemont chemical sedimentary rocks (Fig. 6B).

It is evident that both PCA and hierarchical clustering of variables validate the 18 selected variables as a suitable subcomposition to characterize key rock-forming processes operating at the Rosemont skarn deposit (Figs. 5 and 6B). However, in this study the cluster dendrogram is preferred since it presents the variables in a decision tree form, making it easier to visualize and group variables based on their

similarity.

4.2. Mapping the geochemical space

4.2.1. Exploring geochemical processes in the simplex

The information extracted from the cluster dendrogram (Fig. 5) was used to create composite variables using the geometric mean of the components (Eq. (1), Section 3.2.2) in order to reduce the dimensionality of the 18-part subcomposition used to model the lithogeochemistry of the Rosemont deposit. Accordingly, new 4- and 3-part subcompositions were created to facilitate data visualization using centered tetrahedral and ternary diagrams (Eqs. (2) and (3), Section 3.2.2).

The 4-part subcomposition comprises (1) Ca, (2) Mg, (3) Group 2 variables Cr, Ni, P, Co, and V, and (4) Group 3 variables Hf, Zr, Th, Ti, Al, Nb, Sc, Ta, Y, Ce, and La (Fig. 5). The 3-part subcomposition combines Groups 2 and 3 variables into a single composite variable denoted as Group 4. The resulting 4- and 3-part subcompositions are used to explore and map the geochemical space of the Rosemont deposit in order to select appropriate projections to develop a lithogeochemical model.

Fig. 7 shows a centered tetrahedral diagram of the 4-part subcomposition for the Rosemont deposit. The tetrahedral diagram reveals a rich data structure with at least two major domains. Domain 1 represents a compositional plane that can be projected from the Ca-Mg border into approximately the center of the Group 2-Group 3 border (Fig. 7). This plane represents chemical sedimentary rocks within the Lower Plate of the Rosemont deposit, which contains most of the economic Cu-Mo-Ag mineralization. Domain 2 forms a tighter pattern and can be interpreted as a compositional line controlled dominantly by Groups 2 and 3 variables (Fig. 7). Domain 2 represents siliciclastic sedimentary rocks and crystalline rocks occurring in the Upper Plate and West Block of the Rosemont deposit (Fig. 2).

Domains 1 and 2 have their own internal clusters representing different rock types (Fig. 7). For instance, Domain 1 displays several clusters including those close to the Ca and Mg vertices, respectively representing limestone and dolostone (Fig. 7). Several other clusters away from the Ca-Mg border and closer to the Group 2-Group 3 border represent mixed chemical-siliciclastic sedimentary rocks (Fig. 7). These mixed rocks are represented in the Rosemont deposit by marlstone, calcareous siltstone, and calcareous sandstone (Fig. 4B–C). Domain 2 displays two dominant clusters observed in the tetrahedral diagram (Fig. 7). Andesitic volcanic rocks in the Upper Plate of the Rosemont deposit are represented by the cluster proximal to the Group 2 vertex, whereas the cluster proximal to Group 3 vertex represents siliciclastic sedimentary rocks, porphyries, and other crystalline rocks in the area.

An important observation of the geometry of the geochemical space of the Rosemont deposit displayed in the tetrahedral diagram is that most of the information can be efficiently projected into a centered ternary diagram if Ca and Mg are preserved as independent variables, and Groups 2 and 3 are combined into a single variable denoted as Group 4 (Fig. 8A). The equivalent non-centered ternary diagram is shown on Fig. 8B for comparison and to stress the importance of the centering operation to open up the data structure in the simplex (Section 3.2.2). It is noteworthy that the data structure contained in the ternary diagram is sufficient to discriminate siliciclastic and crystalline

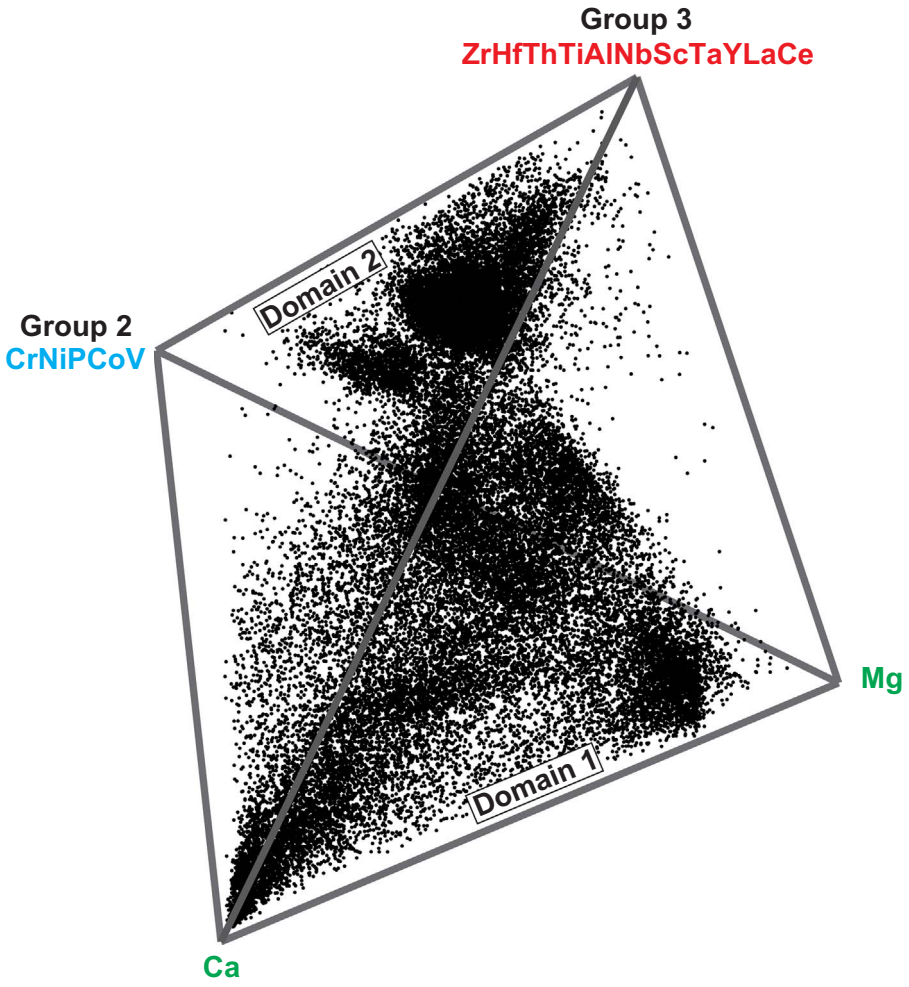

Fig. 7. Centered tetrahedral plot, 4-part simplex, representing an 18-part subcomposition reduced into 4 components. Groups 2 and 3 composite variables were calculated by computing the geometric mean of the parts. The diagram illustrates two major domains. Domain 1 is a compositional plane representing chemical sedimentary rocks within the Lower Plate of the Rosemont deposit. Domain 2 forms a compositional line representing siliciclastic and crystalline rocks present in the Upper Plate and West Block of the deposit. Variables are color coded to facilitate comparison with the cluster dendrogram on Fig. 5.

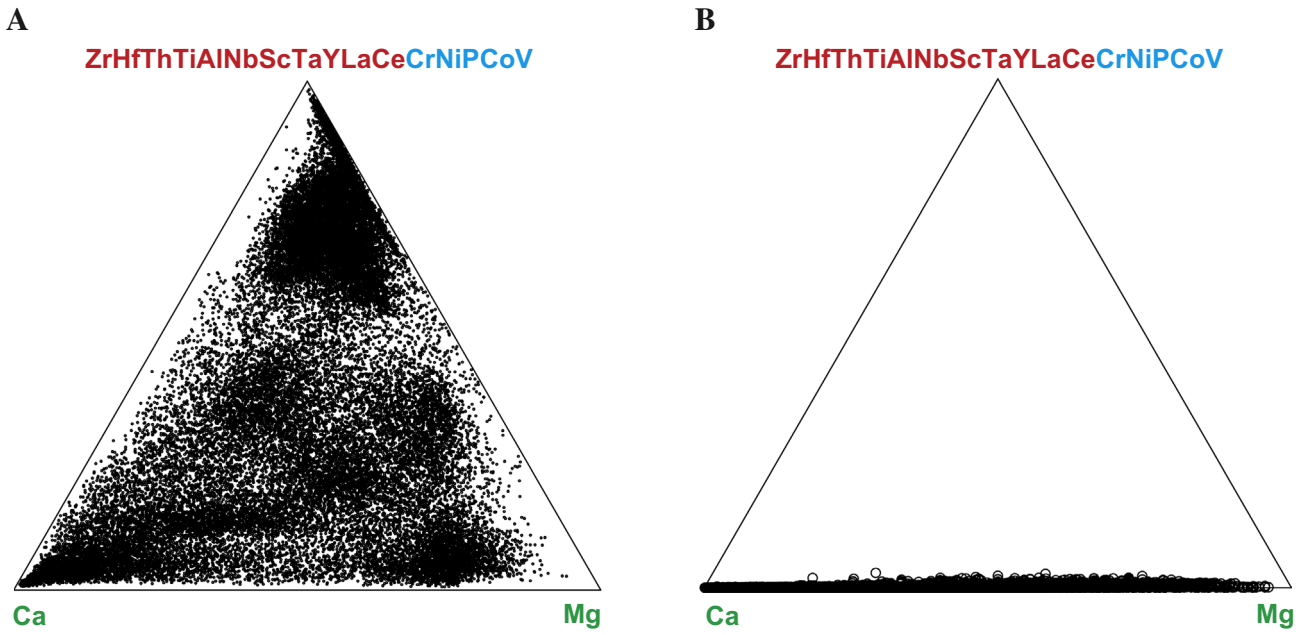

Fig. 8. (A) Centered and (B) non centered ternary diagrams, 3-part simplex, of the Rosemont deposit dataset. The centered ternary diagram reveals a rich data structure indicating that this projection is suitable to map the lithogeochemical attributes of the deposit. The composite variable was calculated by computing the geometric mean of the parts.

rocks from chemical sedimentary rocks. In addition, the chemical sedimentary rocks can also be classified into different subgroups using the same projection (Fig. 8A).

4.2.2. Lithogeochemical classification in the simplex

A major challenge in establishing the lithogeochemical attributes of a mineral deposit is to find a suitable simplicial projection with rich data structure that can be linked to rock-forming processes. In this study, a suitable projection is given by the ternary diagram on Fig. 8A (Section 4.2.1). Empirical lithogeochemical boundaries for the Rosemont skarn deposit were established by mapping high point-density areas on the ternary diagram (Fig. 9). These areas were labelled using a practical nomenclature with 7 classes that are reminiscent of the overall geological processes that may result in the clusters representing each area on Fig. 9.

High point-density areas close to the vertices of the ternary diagram were named limestone, dolostone, and siliciclastic-crystalline classes (Fig. 9). These three classes represent the lithogeochemical end members of the Rosemont skarn deposit comprising relatively pure limestone and dolostone, with minor incorporation of siliciclastic component, as well as all siliciclastic sedimentary rocks and crystalline rocks represented by arkose, conglomerate, porphyry, andesite, and granitoid.

The other four lithogeochemical classes on Fig. 9 represent compositional mixtures of the three lithogeochemical end members described above. These four classes may result from three broad processes. First, primary sedimentary processes such as mixing of chemical and siliciclastic sediments resulting in mixed chemical-siliciclastic rocks such as marlstone, calcareous siltstone, and calcareous sandstone. Second, metasomatic alteration of siliciclastic sedimentary rocks and crystalline rocks driven by the mobility of Ca and Mg. These processes can drive a rock with an initial siliciclastic-crystalline lithogeochemical attribute into a mixed lithogeochemical signature such as siliciclastic-limestone and siliciclastic-dolostone class (Fig. 9). Third, it is unlikely that rocks with primary limestone and dolostone lithogeochemical signatures can be changed into a mixed lithogeochemical class by hydrothermal alteration given that Group 4 chemical elements representing the siliciclastic-crystalline component (S-C) on Fig. 9 are dominantly immobile during hydrothermal alteration (Ludden and Thompson, 1979; Ludden et al., 1982; Ague, 1994; Staudigel et al., 1996; Alt, 1999; Polat and Hofmann, 2003; Polat et al., 2003; Ordóñez-Calderón et al., 2008). However, Ca and Mg losses in limestone and dolostone may drive their composition into a mixed lithogeochemical class.

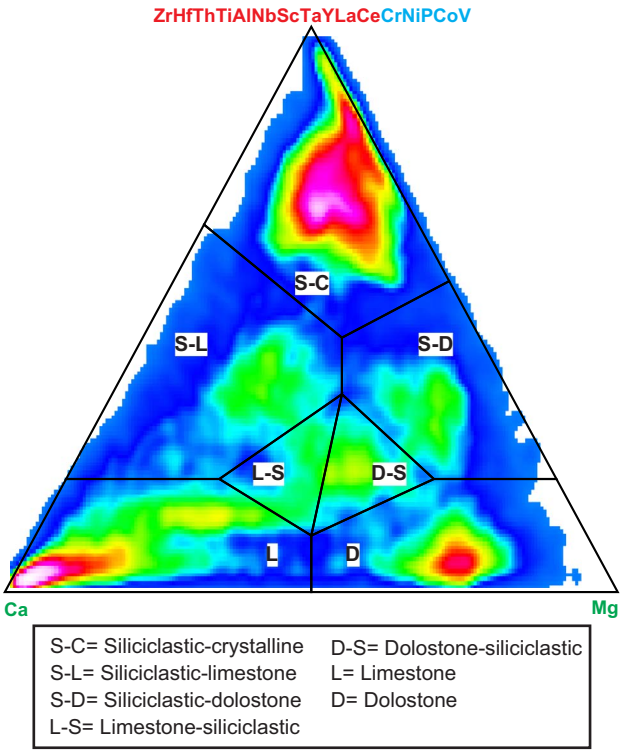

Fig. 9. Centered ternary diagram as shown on Fig. 8A with superposed heat map highlighting high point-density areas. Lithogeochemical classes were assigned by subdividing the geochemical space into empirical domains containing the clusters made evident by the heat map. The composite variable was calculated by computing the geometric mean of the parts. The heat map was generated using the point density tool of ioGAS®.

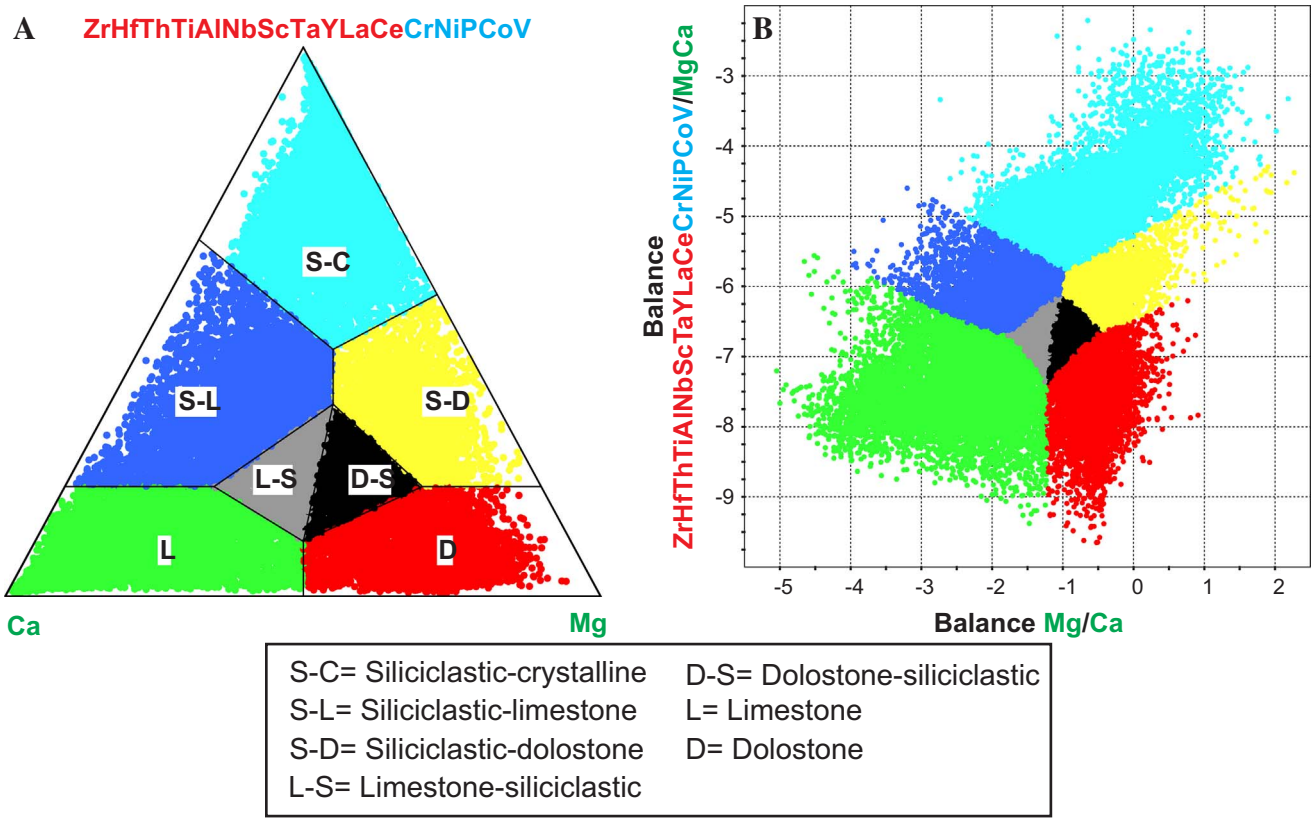

Fig. 10. (A) Ternary diagram or 3-part simplex with observations color coded by lithogeochemical class as defined on Fig. 9. The composite variable was calculated by computing the geometric mean of the parts. (B) Scatter plot of two balances representing ilr-coordinates of the sample space given by the 3-part simplex in (A). The lithogeochemical boundaries are preserved on the scatter plot of ilr-coordinates. This is expected since the 3-part simplex and the ilr-coordinates represent equivalent geochemical spaces. The 2 balances were calculated using Eq. (4).

4.2.3. Classification based on K-means clustering of balances

An alternative approach to define lithogeochemical classes is to conduct a *K*-means cluster analysis of observations based on the 3-part subcomposition represented in the ternary diagram (Fig. 9) to partition the geochemical space into statistical groups. Two balances, ilr-coordinates, were calculated using the 3-part subcomposition (Ca, Mg, and Group 4) represented on Fig. 9 to have an equivalent geochemical space in $\mathbb{R}^2$ for cluster analysis (Eq. (4), Section 3.2.2). The two ilr-variables calculated in this study used the following binary partition: balance 1 [Mg|Ca], and balance 2 [Cr, Ni, P, Co, V, Hf, Zr, Th, Ti, Al, Nb, Sc, Ta, Y, Ce, La | Mg, Ca].

A graphical inspection of the lithogeochemical classification on the ternary diagram (3-part simplex) and the ilr-coordinates ($\mathbb{R}^2$) illustrates the equivalence of these sample spaces (Fig. 10A–B). It is evident that the empirical decision boundaries among different lithogeochemical classes are preserved in the scatter plot of ilr-coordinates (Fig. 10A–B).

A plot of total within-cluster sum of square errors against the number of *K*-clusters suggests at least 4 clusters for the Rosemont deposit (Fig. 11). However, an inspection of the point-density heat map on Fig. 9 suggests 7 to 8 clusters. The challenge of deciding the number of clusters is common. In this study, we seek to find a sensible number of lithogeochemical groups. Thus, we computed a *K*-means clustering with $K = 8$ to compare the cluster analysis with the empirical lithogeochemical boundaries (Fig. 12A). It is evident that clustering balances provides a remarkable similarity with the empirical boundaries chosen based on the point-density heat map (Figs. 9 and 12A). However, there are a few minor differences. First, the siliciclastic-crystalline class is subdivided into two clusters. The lithogeochemical classification of these rocks is not the primary interest since visual discrimination of porphyry, arkose, and conglomerate is a relatively simple task. The goal is to classify chemical sedimentary rocks with various amounts of siliciclastic component and various degrees of dolomitization. Second, the limestone class includes two clusters. *K*-means clustering is very efficient at identifying the purest limestones. Third, the limestone-siliciclastic and dolostone-siliciclastic classes are merged into a single cluster (Fig. 12A). The empirical classification arbitrarily subdivided

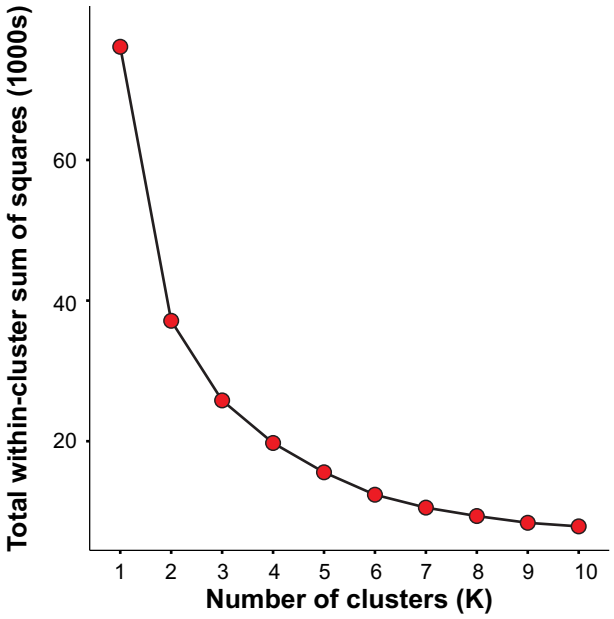

Fig. 11. (A) Total within-cluster sum of squares illustrating the variation of the within-cluster errors as the number of *K* clusters increase.

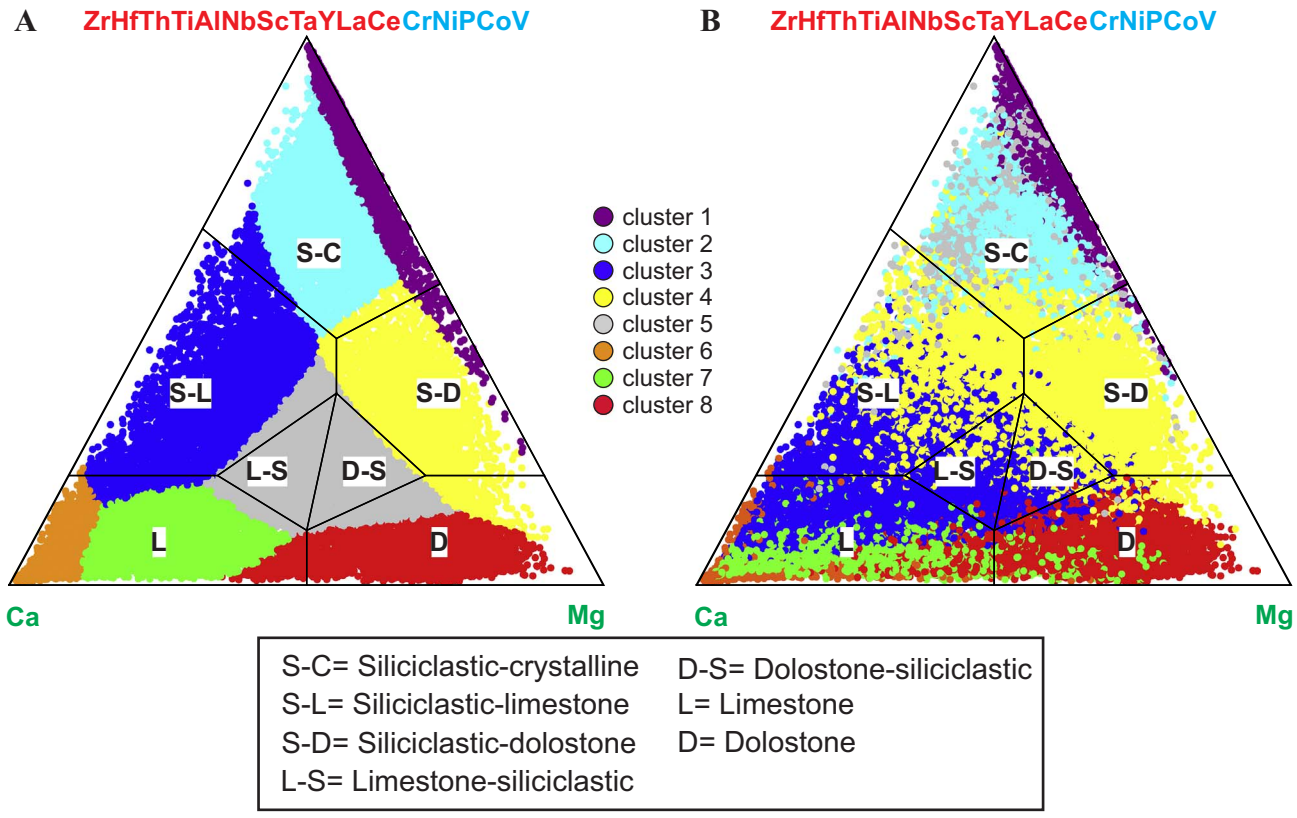

Fig. 12. (A) Ternary diagram or 3-part simplex with observations color coded by cluster after *K*-means clustering of 2 balances (ilr-coordinates) representing the same geochemical space given by the ternary diagram. There is good correspondence between the clusters and the lithogeochemical classes. (B) Ternary diagram with observations color coded by cluster after *K*-means clustering of 17 balances representing the 18 chemical elements used to build the ternary diagram. The clusters have no relationship with the previously defined lithogeochemical boundaries given that the 17 ilr-coordinates represent a geochemical space that is different from that represented in the ternary diagram. The composite variable was calculated by computing the geometric mean of the parts.

Table 3
Contingency table of the conditional probability (%) distribution of lithogeochemical classes given a logged formation P(Lithogeochemistry | Formation). Numbers in bold font to facilitate recognition of the lithogeochemical and stratigraphic associations discussed on Section 4.3

Formation \Lithogeochemistry	Siliciclastic-crystalline	Siliciclastic-dolostone	Siliciclastic-limestone	Limestone	Limestone-siliciclastic	Dolostone	Dolostone-siliciclastic	Total (%)
Gila Conglomerate	**99.9**	0.1	0.0	0.0	0.0	0.0	0.0	100
Porphyry	**92.4**	1.7	5.1	0.2	0.1	0.2	0.3	100
Andesite	**95.2**	0.8	3.1	0.4	0.4	0.1	0.1	100
Willow Canyon	**97.6**	0.4	1.8	0.0	0.1	0.0	0.1	100
Glance	1.2	0.6	3.2	**75.0**	11.3	4.7	4.0	100
Rainvalley	0.0	0.0	0.0	**85.7**	0.0	14.3	0.0	100
Concha	1.7	1.5	4.0	**82.0**	2.1	7.3	1.5	100
Scherrer	14.6	**35.3**	**21.2**	2.9	7.1	9.4	9.4	100
Epitaph	2.2	9.1	8.6	19.8	2.9	**53.6**	3.8	100
Colina	0.6	1.5	0.8	**54.9**	0.9	**39.2**	2.1	100
Earp	5.4	**57.6**	20.4	3.3	3.3	4.6	5.4	100
Horquilla	2.9	6.1	**27.9**	**34.0**	9.9	5.5	13.6	100
Escabrosa	0.7	2.4	8.6	**72.0**	2.9	9.1	4.3	100
Martin	3.0	2.5	11.7	18.4	2.6	**57.3**	4.6	100
Abrigo	14.5	0.6	**54.2**	13.0	6.4	7.7	3.7	100
Bolsa Quartzite	**90.8**	1.5	1.1	1.1	4.4	0.0	1.1	100
Precambrian Granitoids	**98.8**	0.9	0.3	0.0	0.0	0.0	0.0	100
Undifferentiated	**27.8**	6.3	14.7	**23.9**	3.4	19.9	4.0	100

this field to document differences in the Mg/Ca ratio to monitor the presence of Mg-rich clay minerals, which have deleterious effects in metal recoveries (Wang et al., 2015b, 2016a, 2016b).

To stress the importance of working in the appropriate geochemical space in lithogeochemical classification, we have computed *K*-means clustering, $K = 8$, on a data matrix of 17 balances derived from the 18-parts subcomposition used in this study (Fig. 12B). On Fig. 12B, it is evident that clustering 17 balances result in groups that are not directly related to the lithogeochemical classes defined on the 3-part simplex, or by clustering 2 balances representing the same variables of the 18-parts subcomposition reduced into a lower dimensional space (Fig. 12). This difference is expected since the data matrices of 2 and 17 balances represent different geochemical spaces. Although the validity of the clusters defined by the 17 balances is not in question, these clusters gather mixed information that is of no practical use to establish a lithogeochemical model that is simple to associate with rock types and

rock-forming processes. Clustering geochemical spaces designed to investigate specific geological attributes, such as lithogeochemistry (e.g., Fig. 9), has the advantage of providing direct geological meaning to the clusters instead of being a simple exercise on pattern recognition.

For practical purposes in this study, we have adopted the empirical lithogeochemical classification defined on the 3-part simplex. *K*-means clustering of the equivalent geochemical space was used to validate the proposed classification (Fig. 12A). However, in complex geological situations in which subcompositions with > 4 components are needed to explain the lithogeochemical variability, empirical boundaries are not possible given that these high-dimensional subcompositions cannot be represented graphically. In such cases, *K*-means clustering of balances representing the same geochemical space are a good tool for classification.

Table 3 presents a contingency table of the conditional probability distribution of the lithogeochemical classes given a formation logged on drill core, denoted as P(Lithogeochemistry | Formation) and expressed in percentage. The conditional probability distribution demonstrates the association of the lithogeochemical classes with the formations present at the Rosemont deposit. For instance, the siliciclastic-crystalline class is the dominant lithogeochemical attribute of formations in the Upper Plate and West Block including Precambrian Granitoids, Bolsa Quartzite, Willow Canyon arkose and andesite, Gila Conglomerate, as well as porphyritic intrusions (Figs. 2–3). Notably, regional dolomitization trends are commonly associated with Martin, Colina, and Epitaph Formations, which is clearly documented by the conditional probabilities of the lithogeochemical model (Table 3) (cf., Johnson and Ferguson, 2007; Ferguson, 2009; Ferguson et al., 2009; Rasmussen et al., 2012). The siliciclastic-dolostone class characterizes the Earp Formation, which is consistent with field descriptions indicating a mixed chemical-siliciclastic composition. It is noteworthy that regional stratigraphic studies indicate that the Escabrosa and Horquilla Formations consist of limestone packages with increasing siliciclastic component towards the top of Horquilla; a feature well documented by the lithogeochemical model in which the conditional probability of the siliciclastic-limestone class increases from Escabrosa to Horquilla (Table 3) (*op. cit.*). It is concluded that the lithogeochemical model is a valid geochemical tool to map the lithological attributes of the Rosemont deposit.

4.3. Mapping the geospace

The lithogeochemical model devised in this study was used to map the geological space of the Rosemont skarn deposit in order to create a simplified chemostratigraphy to better understand the geological attributes of the deposit. Fig. 13 shows a vertical section of the deposit representing 90 diamond drill holes with 33,000 samples color coded by lithogeochemical class to visualize the spatial variability and to reveal the structural architecture of the deposit (Fig. 13).

The spatial distribution of the lithogeochemical classes clearly map the three major structural domains of the deposit (Fig. 13, Table 3): (1) the Upper Plate, dominated by the siliciclastic-crystalline class representing arkose, andesite, and conglomerate, (2) the West Block, evident by a sliver of rocks with siliciclastic-crystalline class attributes representing granitoid and quartzite interleaved with dolostone, limestone, and siliciclastic-limestone classes, and (3) the Lower Plate, the major host of economic mineralization, discriminated by class attributes such as limestone, dolostone, and all classes representing mixed chemical-siliciclastic sediments (Fig. 9). The lithogeochemical classes reveal the east-dipping homoclinal structure that characterizes the Lower Plate of the Rosemont deposit (Figs. 2 and 13).

The spatial distribution of the lithogeochemical classes within the Lower Plate suggests sedimentation cycles with increasing siliciclastic component towards the top of the east-dipping chemical sedimentary succession (Fig. 13, Table 3). The Lower Plate succession ranges from relatively clean limestone at the base, followed by increased mixing between chemical and siliciclastic component to the east and higher-up in the stratigraphy, to relatively clean dolostone and minor limestone in the uppermost part of the stratigraphy (Fig. 13). These sedimentation cycles are well documented in the area and have been attributed to marine regression and transgression events (e.g., Rasmussen et al., 2012). The geological characteristics described above validate the lithogeochemical model presented on Fig. 9 as a tool to map primary lithological features in strongly calc-silicate altered rocks.

The lithogeochemical model proposed here correctly identifies structural domains, lithological units, and rock-forming processes. A simplified chemostratigraphic model, using Leapfrog Geo®, was developed for the Lower Plate based on the lithogeochemical model. The siliciclastic-dominated Upper Plate was not subdivided given that most of the economic Cu, Mo, and Ag mineralization is hosted in the Lower Plate. Also, the visual identification of rock types in the Upper Plate is relatively simple compared to the identification of the complex lithologies in the Lower Plate.

From a mining perspective, the advantage of an informal mine chemostratigraphy over conventional stratigraphic models is that lithological, mineralogical, and geochemical variability is reduced within the geochemically-driven domains, which has immediate applications in resource modelling and geometallurgical characterization (cf., Gregory et al., 2013; Lund et al., 2013; Amer et al., 2014; Pownceby and Johnson, 2014; Yildirim et al., 2014; Maydagán et al., 2016). Accordingly, the stratigraphy of the Lower Plate of the Rosemont deposit was subdivided into three chemostratigraphic units from bottom to top (1) Lower Limestone Unit, (2) Mixed Unit, and (3) Upper Dolostone Unit (Fig. 14). The deposit simplified chemostratigraphy is well correlated with the regional stratigraphy. For instance, the Lower Limestone Unit is mostly related to the top of Escabrosa and the base of Horquilla composed dominantly of bedded limestone. The Mixed Unit is strictly associated with the Earp Formation and the upper most part of Horquilla comprising dominantly siliciclastic and mixed chemical-siliciclastic sedimentary rocks. The Upper Dolostone Unit is associated with the Epitaph Group, which is dominated by dolomite, evaporatic rock, and minor limestone (Table 3, Figs. 2, 3, and 14).

4.4. Lithogeochemical relationships with ore grades

An important relationship revealed by the lithogeochemical model is a strong association of the mineralization with the lithogeochemical classes. Fig. 15 shows copper grades for samples with > 1000 ppm Cu to exclude non-economic mineralization. Lithogeochemical classes representing relatively clean chemical sedimentary rocks such as dolostone, limestone, and limestone-siliciclastic (Escabrosa, Horquilla, and Epitaph Group) are associated with higher copper grades, than those of mixed chemical-siliciclastic rocks (Earp Formation) such as siliciclastic-crystalline, siliciclastic-limestone, and siliciclastic-dolostone classes (Fig. 15). The dolostone-siliciclastic class display lower grades than its limestone-siliciclastic counterpart, most likely indicating the presence of a larger amount of siliciclastic component.

The relationship of ore grades with the lithogeochemical classes provides an important tool for exploration of skarn deposits. This relationship is explained in terms of the receptivity of sedimentary rocks to be mineralized at metal grades of economic value. Accordingly, chemical sedimentary rocks relatively clean of siliciclastic component are more fertile for economic skarn mineralization than their mixed chemical-siliciclastic counterparts. This explains well the fact that the Earp Formation hosts the lower copper grades of the Rosemont deposit.

We suggest that the lithogeochemical model devised in this study (Fig. 9) can also be used as a geochemical exploration tool to assess and map the skarn fertility of chemical-siliciclastic sedimentary successions in areas permissive of skarn mineralization.

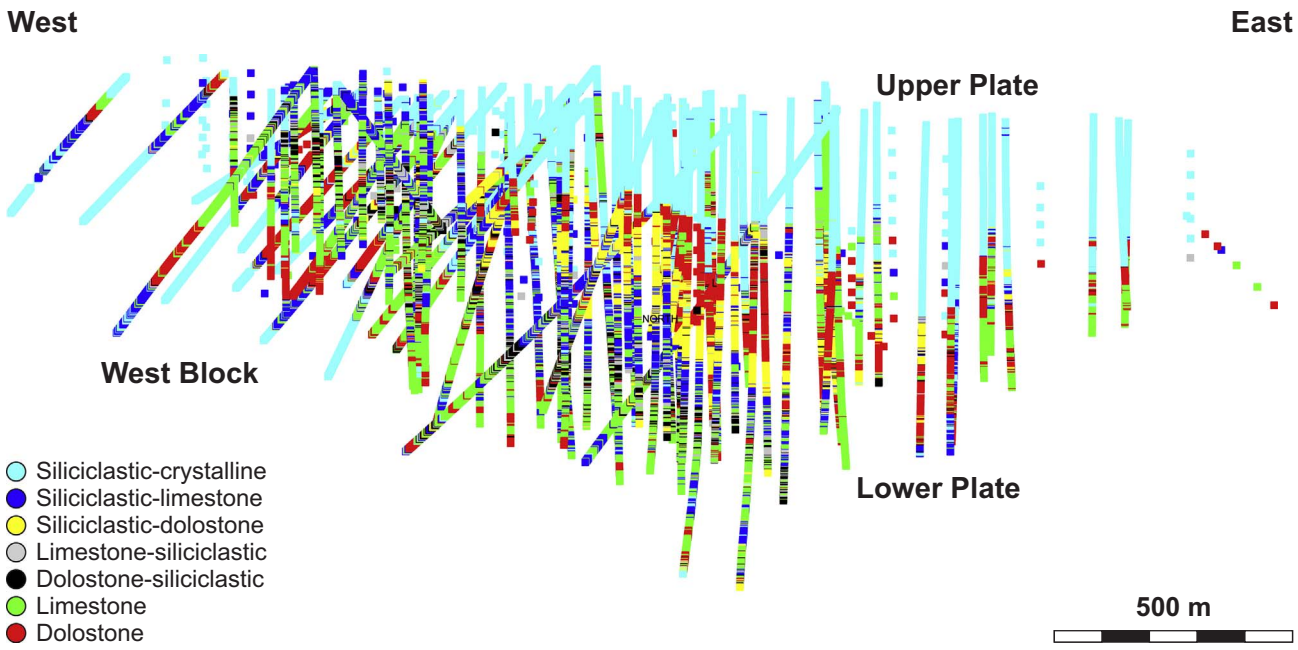

Fig. 13. East-West vertical section projecting 90 diamond drill holes sampled along the entire core length and analyzed for multi-element geochemistry. The section contains 33,000 samples color coded by lithogeochemical class (Fig. 9). The lithogeochemical classification devised in this study discriminates the Upper Plate, Lower Plate, and West Block. Also, the east-dipping homoclinal structure of the Lower Plate is well documented.

5. Conclusions

Establishing a reliable stratigraphic model for a skarn deposit is important for planning and developing a mining operation given that stratigraphic domains play a key role in resource modelling, geometallurgical characterization of ore bodies, and several other mining parameters. However, complex geological attributes of skarn deposits including metasomatic alteration and lithological variability complicates the development of stratigraphic models based on traditional core logging observations. To circumvent these problems, we presented a systematic approach to develop a lithogeochemical model that can be used as the framework for establishing a simplified chemostratigraphy. We applied the principles of compositional data analysis and multivariate statistics to 4-acid digested multi-element geochemical data of the Rosemont Cu-Mo-Ag skarn deposit reaching the following conclusions:

1. Selection of a subcomposition with elements that are immobile during metasomatic alteration is critical for lithogeochemical modelling. In this study, an 18-part subcomposition including Ca, Mg, Cr, Ni, P, Co, V, Hf, Zr, Th, Ti, Al, Nb, Sc, Ta, Y, Ce, and La was selected to minimize the effects of alteration on lithological discrimination. Mobile elements Ca and Mg were included in the analysis to represent limestone and dolostone.
2. An efficient exploratory data analysis technique is the application of hierarchical clustering of geochemical variables using the variation matrix (Section 4.1.1). The cluster dendrogram (Fig. 5) resulting from this approach is a critical tool to make data-driven decisions on grouping variables to reduce dimensionality and to explore projections in the simplex.

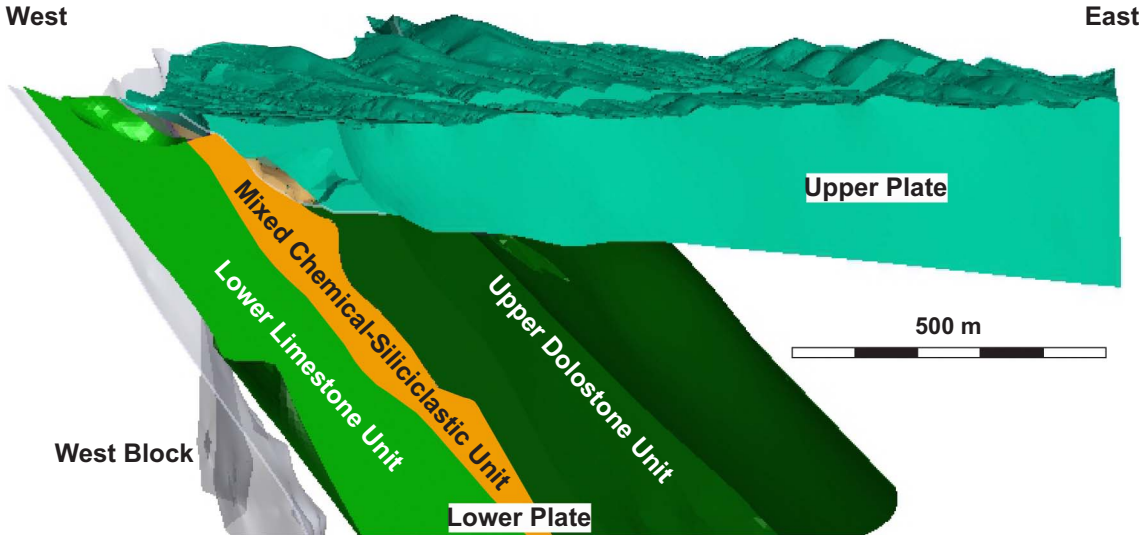

Fig. 14. Three dimensional model with the proposed chemostratigraphy for the Rosemont deposit based on the lithogeochemical classes (Figs. 9 and 13). The Lower Plate of the Rosemont deposit contains most of the economic Cu, Mo, and Ag mineralization. The stratigraphy of the Lower Plate can be simplified into a Lower Limestone Unit, a Mixed Unit of chemical-siliciclastic sedimentary rocks, and an Upper Dolostone Unit.

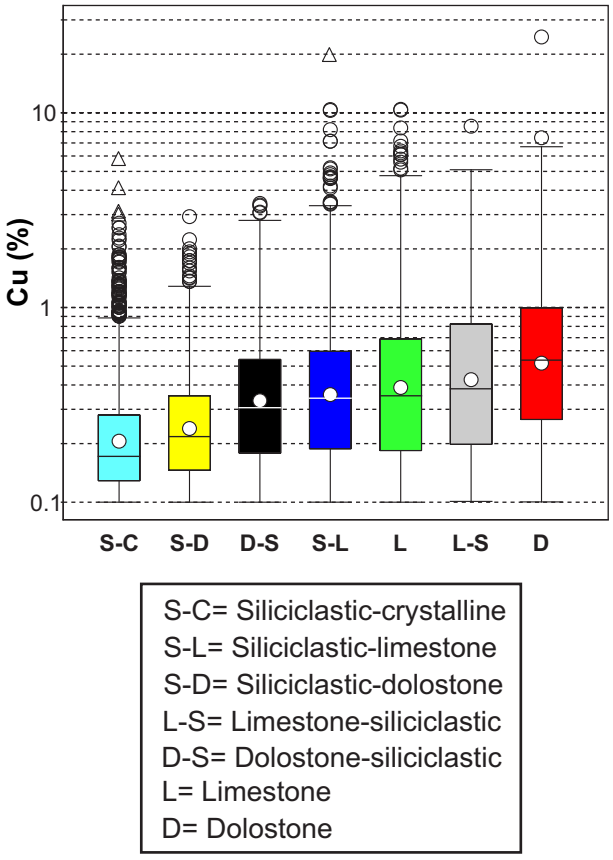

Fig. 15. Box plot illustrating the relationships between Cu grades and the lithogeochemical classes devised in this study. It is noteworthy that the lithogeochemical classes representing relatively pure chemical sedimentary rocks tend to contain higher copper grades than those classes representing siliciclastic and impure chemical-siliciclastic rocks. The mean is represented by the white circle and the median by the black horizontal line within the box.

3. Understanding the geometry of the geochemical space represented by a particular subcomposition is critical to select the appropriate projections to discover geological processes encrypted in the geochemical data. Provided that an appropriate projection is found, mapping the geochemical space to produce a lithogeochemical model is a relatively simple task that may be accomplish in a lower dimensional space. For instance, a ternary diagram contains enough information to map the lithogeochemical attributes of sedimentary rocks of the Rosemont skarn deposit (Fig. 9).
4. Empirical decision boundaries to subdivide a ternary diagram into lithogeochemical classes were established by grouping regions with high-point density using heat maps (Fig. 9). Comparable decision boundaries can be obtained by computing *K*-means clustering on a data matrix of 2 balances representing a sample space equivalent to the ternary diagram or 3-part simplex (Fig. 12A).
5. The empirical approach of dividing the geochemical space works well in low dimensional spaces in which all variables can be visualized graphically. In higher dimensional spaces *K*-means clustering is an appropriate solution. However, clustering should be done on balances representing the equivalent geochemical space of a given *D*-part simplex. Otherwise, regions in the simplex will not correspond with the clusters obtained from *K*-means clustering (Fig. 12, Section 4.2.3).
6. Geospatial plots of the lithogeochemical classes effectively recognize the three major structural domains of the Rosemont deposit: Upper Plate, Lower Plate, and West Block (cf., Figs. 2 and 13). In addition, the east-dipping homoclinal structure of the Lower Plate is also well documented by the lithogeochemistry (Fig. 13). A simplified chemostratigraphy can be defined by spatially grouping the lithogeochemical units into a Lower Limestone Unit, overlaid by a Mixed Unit of chemical-siliciclastic sedimentary rocks, and an Upper Dolostone Unit (Fig. 14). These three chemostratigraphic units correlate well with the regional stratigraphy, respectively, the Escabrosa, Horquilla, and Earp Formations, and the Epitaph Group.
7. A significant implication of the lithogeochemical model is the strong association of copper grades with lithogeochemical classes (Fig. 15). This suggests that the receptivity of different rock types to uptake copper mineralization is dependent on the proportion of chemical and siliciclastic component. Accordingly, relatively clean chemical sedimentary rocks with low siliciclastic component have higher potential of hosting economic mineralization in geological environments permissive of skarn deposits. This finding suggests that the lithogeochemical model can be used as a skarn fertility tool to evaluate the economic potential of chemical-siliciclastic sedimentary successions.

Acknowledgments

We thank Geologists Jeff Cornoyer and David Young for sharing their knowledge of the Rosemont deposit and for their hard work during two drilling programs conducted by Hudbay. Thanks to Structural Geologist David Lewis for enlightening us on the structural architecture of the Rosemont deposit. We are very thankful with Hudbay Minerals Inc., for allowing us to publish this scientific contribution. Dr. Jamil Sader (Corporate geochemist) and Brooke Mills (Geologist and Account Manager) from Bureau Veritas are thanked for kindly implementing all laboratory technical requests to ensure a successful geochemical program. This manuscript significantly improved thanks to insightful revisions by Dr. Raimon Tolosana-Delgado, Dr. John Carranza, and an anonymous reviewer. Thanks to Professor Stefano Albanese, Editor, Journal of Geochemical Exploration, for considering this manuscript for publication.

References

Ague, J.J., 1994. Mass transfer during Barrovian metamorphism of pelites, south-central Connecticut I: Evidence for changes in composition and volume. Am. J. Sci. 294, 989–1057.
Aitchison, J., 1986. The statistical analysis of compositional data. In: Monographs on Statistics and Applied Probability. Chapman & Hall, London, pp. 416.
Aitchison, J., Egozcue, J.J., 2005. Compositional data analysis: where are we and where should we be heading? Math. Geol. 37 (7), 829–850.
Aitchison, J., Greenacre, M., 2002. Biplots of compositional data. Appl. Stat. Series C 51 (4), 375–392.
Aitchison, J., Barceló-Vidal, C., Egozcue, J.J., Pawlowsky-Glahn, V., 2002. A concise guide for the algebraic-geometric structure of the simplex, the sample space for compositional data analysis. In: Bayer, U., Burger, H., Skala, W. (Eds.), Proceedings of IAMG'02-The eight annual conference of the International Association for Mathematical Geology. vols. I and II. pp. 387–392.
Alt, J.C., 1999. Hydrothermal alteration and mineralization of oceanic crust: mineralogy, geochemistry, and processes. In: Barrie, C.T., Hannington, M.D. (Eds.), Volcanic-Associated Massive Sulphide Deposits: Processes and Examples in Modern and Ancient Settings. Reviews in Economic Geology Vol. 8. pp. 133–155.
Amer, T.E., El Assay, I.E., Rezk, A.A., El Kammar, A.M., El Manawi, A.W., Abu Khoziem, H.A., 2014. Geometallurgy and processing of North Ras Mohamed poly-mineralized ore materials, South Sinai, Egypt. Int. J. Miner. Process. 129, 12–21.
Baghban, S., Hosseinzadeh, M.R., Moayyed, M., Mokhtari, M.A.A., Gregory, D.D., Nia, H.M., 2016. Chemical composition and evolution of the garnets in the Astamal Fe-LREE distal skarn deposit, Qara-Dagh–Sabalan metallogenic belt, Lesser Caucasus, NW Iran. Ore Geol. Rev. 78, 166–175.
Barceló-Vidal, C., Martín-Fernández, J.A., 2016. The mathematics of compositional analysis. Aust. J. Stat. 45, 57–71.
Barceló-Vidal, C., Martín-Fernández, J.A., Pawlowsky-Glahn, V., 2001. Mathematical foundations of compositional data analysis. In: Ross, G. (Ed.), Proceedings of IAMG'01-The Sixth Annual Conference of the International Association for Mathematical Geology, 20, (CD-ROM).
Bhatia, M.R., Crook, K.A.W., 1986. Trace element characteristics of graywackes and tectonic setting discrimination of sedimentary basins. Contrib. Mineral. Petrol. 92 (2), 181–193.
Buccianti, A., Nisi, B., Raco, B., 2016. Towards the concept of background/baseline compositions: A practicable path? In: Martín-Fernández, J.A., Thió-Henestrosa, S. (Eds.), Compositional Data Analysis. Springer Proceedings in Mathematics and

Statistics Vol. 187. pp. 31–43.
Caja, M.A., Marfil, R., Lago, M., Salas, R., Ramseyer, K., 2007. Provenance discrimination of Lower Cretaceous synrift sandstones (eastern Iberia Chain, Spain): constraints from detrital modes, heavy minerals, and geochemistry. In: Arribas, J., Critelli, S., Johnsson, M.J. (Eds.), Sedimentary Provenance and Petrogenesis: Perspectives from Petrography and Geochemistry. Geological Society of America Special Paper Vol. 420. pp. 181–197.
Chayes, F., 1960. On correlation between variables of constant sum. J. Geophys. Res. 65 (12), 4185–4193.
Chayes, F., 1971. Ratio Correlation. University of Chicago Press, Chicago, IL, pp. 99.
Chayes, F., 1975. A priori and experimental approximation of simple ratio correlations. In: McCammon, R.B. (Ed.), Concepts in Geostatistics. Springer, pp. 106–137.
Core Team, R., 2017. R: A Language and Environment for Statistical Computing. R Foundation for Statistical Computing, Vienna, Austria. https://www.r-project.org/.
Davies, J.C., 2002. Statistics and Data Analysis in Geology, third ed. John Wiley and Sonspp. 638.
Deng, X.-D., Li, J.-W., Wen, G., 2015. U-Pb geochronology of hydrothermal zircons from the early Cretaceous iron skarn deposits in the Handan-Xingtai district, North China Craton. Econ. Geol. 110, 2159–2180.
Drewes, H., 1971. Mesozoic stratigraphy of the Santa Rita Mountains, southeast of Tucson, Arizona. In: U.S. Geological Survey Professional Paper. 658-C. pp. 81.
Drewes, H., 1972a. Cenozoic rocks of the Santa Rita Mountains, southeast of Tucson, Arizona. In: U.S. Geological Survey Professional Paper. 746. pp. 66.
Drewes, H., 1972b. Structural geology of the Santa Rita Mountains, southeast of Tucson, Arizona. In: U.S. Geological Survey Professional Paper. 748. pp. 35.
Egozcue, J.J., Pawlowsky-Glahn, V., 2005. Groups of parts and their balances in compositional data analysis. Math. Geol. 37 (7), 795–828.
Egozcue, J.J., Pawlowsky-Glahn, V., 2006. Simplicial geometry for compositional data. In: Buccianti, A., Mateu-Figueras, G., Pawlowsky-Glahn, V. (Eds.), Compositional Data Analysis in the Geosciences: From Theory to Practice. Geological Society, London, Special Publications Vol. 264. pp. 145–159.
Egozcue, J.J., Pawlowsky-Glahn, V., Mateu-Figueras, G., Barceló-Vidal, C., 2003. Isometric logratio transformations for compositional data analysis. Math. Geol. 35 (3), 279–300.
Einaudi, M.T., Burt, D.M., 1982. Introduction: Terminology, classification, and composition of skarn deposits. A special issue devoted to skarn deposits. Econ. Geol. 77, 745–754.
Einaudi, M.T., Meinert, L.D., Newberry, R.J., 1981. Skarn deposits. In: Economic Geology 75th Anniversary Volume, pp. 317–391.
Fedo, C.M., Nesbitt, H.W., Young, G.M., 1995. Unraveling the effects of potassium metasomatism in sedimentary rocks and paleosols, with implications for paleoweathering conditions and provenance. Geology 23 (10), 921–924.
Ferguson, C.A., 2009. Bedrock geologic map of the Northern Part of the Empire Ranch 7 ½' Quadrangle, Pima County, Arizona. In: Arizona Geological Survey Open-File Report OFR-09-05, (scale 1:24,000).
Ferguson, C.A., Johnson, B.J., Pearthree, P.A., Spencer, J.E., Shipman, T.C., Cook, J.P., 2009. Geologic map of the Helvetia 7½' quadrangle, Pima County, Arizona. In: Arizona Geological Survey Open-File Report, (09–06, scale 1:24,000).
Gabriel, K.R., 1971. The biplot graphic display of matrices with application to principal component analysis. Biometrika 58 (3), 453–467.
Gaspar, L.M., Inverno, C.M., 2000. Mineralogy and metasomatic evolution of distal strata-bound scheelite skarns in the Riba de Alva Mine, Northeastern Portugal. Econ. Geol. 95, 1259–1275.
Gower, J.C., Hand, D.J., 1996. Biplots. Chapman and Hallpp. 271.
Gower, J.C., Gardner-Lubbe, S., Roux, N.L., 2011. Understanding biplots. John Wiley and Sons, Ltd.pp. 463.
Gregory, M.J., Lang, J.R., Gilbert, S., Hoal, K.O., 2013. Geometallurgy of the pebble porphyry copper-gold-molybdenum deposit, Alaska: Implications for gold distribution and paragenesis. Econ. Geol. 108, 463–482.
Grunsky, E.C., 2010. The interpretation of geochemical survey data. Geochem. Explor. Environ. Anal. 10, 27–74.
Harris, N.B.W., Pearce, J.A., Tindle, A.G., 1986. Geochemical characteristics of collision-zone magmatism. In: Coward, M.P., Reis, A.C. (Eds.), Collision Tectonics. Geological Society, London, Special Publications Vol. 19. pp. 67–81.
Hartigan, J.A., Wong, M.A., 1979. A *K*-means clustering algorithm. J. R. Stat. Soc.: Ser. C: Appl. Stat. 28 (1), 100–108.
Helsel, D.R., 2012. Statistics for Censored Environmental Data Using Minitab® and R, second ed. John Wiley & Sons, Inc., Hoboken, New Jersey, USA (324 p).
Husson, F., Lê, S., Pagès, J., 2011. Exploratory Multivariate Analysis by Example Using R. CRC Press, Taylor and Francis Group, pp. 224.
Irving, T.N., Baragar, W.R.A., 1971. A guide to the chemical classification of the common volcanic rocks. Can. J. Earth Sci. 8, 523–548.
Johnson, B.J., Ferguson, C.A., 2007. Geologic map of the Rosemont area, northern Santa Rita Mountains, Pima County, Arizona. In: Arizona Geological Survey Digital Geologic Map DGM-59, ver. 1.1, pp. 10.
Jolliffe, I.T., 2002. Principal Component Analysis, Second Ed. Springerpp. 487.
Keith, S.B., Wilt, J.C., 1986. Laramide orogeny in Arizona and adjacent regions: A stratotectonic synthesis. In: Beatty, B., Wilkinson, P.A.K. (Eds.), Frontiers in Geology and Ore Deposits of Arizona and the Southwest. Arizona Geological Society Digest Vol. 16. pp. 502–554.
Kelemen, P.B., Hanghøj, K., Greene, A.R., 2003. One view of the geochemistry of subduction-related magmatic arcs, with emphasis on primitive andesite and lower crust. In: Holland, H.D., Turekian, K.K. (Eds.), Treatise on Geochemistry. Volume 3. Elsevier, Amsterdam, pp. 593–659.
Kemp, A.I.S., Hawkesworth, C.J., 2003. Granitic perspectives on the generation and secular evolution of the continental crust. In: Holland, H.D., Turekian, K.K. (Eds.), Treatise on Geochemistry. Volume 3. Elsevier, Amsterdam, pp. 349–410.
Li, C., Ren, T., Huang, J.-G., Han, R.-S., Yin, H.-J., Zhou, H.-Y., Feng, Z.-H., 2017. Skarn mineralogy and its geological significance for the Tayuan (Cu–Mo)–Pb–Zn deposit, northern Daxinganling metallogenic belt. Acta Geoch. 36 (1), 89–101.
Lieben, F., Moritz, R., Fontboté, L.L., 2000. Mineralogy, geochemistry, and age constraints on the Zn-Pb skarn deposit of Maria Cristina, Quebrada Galena, Northern Chile. Econ. Geol. 95, 1185–1196.
Ludden, J.N., Thompson, G., 1979. An evaluation of the behavior of the rare earth elements during the weathering of sea-floor basalts. Earth Planet. Sci. Lett. 43, 85–92.
Ludden, J.N., Gélinas, L., Trudel, P., 1982. Archean metavolcanics from the Rouyn-Noranda district, Abitibi greenstone belt, Québec – 2, mobility of trace elements and petrogenetic constraints. Can. J. Earth Sci. 19, 2276–2287.
Lund, C., Lamberg, P., Lindberg, T., 2013. Practical way to quantify minerals from chemical assays at Malmberget iron ore operations – An important tool for the geometallurgical program. Miner. Eng. 49, 7–16.
MacLean, W.H., Barrett, T.J., 1993. Lithogeochemical techniques using immobile elements. J. Geochem. Explor. 48, 109–133.
MacQueen, J., 1967. Some methods for classification and analysis of multivariate observations. In: Le Cam, L.M., Neyman, J. (Eds.), Proceedings of the Fifth Berkeley Symposium on Mathematical Statistics and Probability. Volume 1. Berkeley University of California Press, pp. 281–297.
Martín-Fernández, J.A., Barceló-Vidal, C., Pawlowsky-Glahn, V., 1998. A critical approach to non-parametric classification of compositional data. In: Rizzi, A., Vichi, M., Bock, H.-H. (Eds.), Advances in Data Science and Classification. Springer, pp. 49–56.
Martín-Fernández, J.A., Barceló-Vidal, C., Pawlowsky-Glahn, V., 2003. Dealing with zeros and missing values in compositional data sets using nonparametric imputation. Math. Geol. 35 (3), 253–278.
Mateu-Figueras, G., 2003. Models de distribució sobre el símplex. Ph.D. Thesis. Universitat Politècnica de Catalunya, Barcelona, Spain.
Maydagán, L., Franchini, M., Lentz, D., 2016. Phyllosilicates geochemistry and distribution in the Altar porphyry Cu-(Au) deposit, Andes Cordillera of San Juan, Argentina: Applications in exploration, geothermometry, and geometallurgy. J. Geochem. Explor. 167, 83–109.
McLennan, S.M., 2001. Relationships between the trace element composition of sedimentary rocks and upper continental crust. Geochem. Geophys. Geosyst. 2 (Paper number 2000GC000109).
Meinert, L.D., 1992. Skarns and skarn deposits. Geosci. Can. 19 (4), 145–162.
Meinert, L.W., Lentz, D.R., Newberry, R., 2000. Introduction. A special issue devoted to skarn deposits. Econ. Geol. 95, 1183–1184.
Meschede, M., 1986. A method of discriminating between different types of mid-ocean ridge basalts and continental tholeiites with the Nb-Zr-Y diagram. Chem. Geol. 56, 207–218.
Miller, W.E., 2002. Revisiting the geometry of a ternary diagram with the half-taxi metric. Math. Geol. 34 (3), 275–290.
Mullen, E.D., 1983. $MnO/TiO_2/P_2O_5$: A minor element discriminant for basaltic rocks of oceanic environments and its implications for petrogenesis. Earth Planet. Sci. Lett. 62 (1), 53–62.
Mungal, J.E., 2014. Geochemistry of magmatic ore deposits. In: Scott, S.D. (Ed.), Treatise on Geochemistry, second ed. Volume 13. Elsevier, Amsterdam, pp. 195–218.
Nesbitt, H.W., Young, G.M., 1984. Prediction of some weathering trends of plutonic and volcanic rocks based on thermodynamic and kinetic considerations. Geochim. Cosmochim. Acta 48, 1523–1534.
Nesbitt, H.W., Young, G.M., 1989. Formation and digenesis of weathering profiles. J. Geol. 97 (2), 129–147.
Ohta, T., Arai, H., 2007. Statistical empirical index of chemical weathering in igneous rocks: a new tool for evaluating the degree of weathering. Chem. Geol. 240, 280–297.
Ordóñez-Calderón, J.C., Polat, A., Fryer, B.J., Gagnon, J.E., Raith, J.G., Appel, P.W.U., 2008. Evidence for HFSE and REE mobility during calc-silicate metasomatism, Mesoarchean (~3075 Ma) Ivisaartoq greenstone belt, southern West Greenland. Precambrian Res. 161, 317–340.
Ordóñez-Calderón, Lafrance, B., Gibson, H.L., Schwartz, T., Pehrsson, S.J., Rayner, N.M., 2016. Petrogenesis and geodynamic evolution of the Paleoproterozoic (~1878 Ma) Trout Lake volcanogenic massive sulfide deposit, Flin Flon, Manitoba, Canada. Econ. Geol. 111, 817–847.
Palarea-Albaladejo, J., Martín-Fernández, J.A., 2013. Values below detection limit in compositional chemical data. Anal. Chim. Acta 764, 32–43.
Palarea-Albaladejo, J., Martín-Fernández, J.A., 2015. zCompositions – R package for multivariate imputation of left-censored data under a compositional approach. Chemom. Intell. Lab. Syst. 143, 85–96.
Palarea-Albaladejo, J., Martín-Fernández, J.A., Buccianti, A., 2014. Compositional methods for estimating elemental concentrations below the limit of detection in practice using R. J. Geochem. Explor. 141, 71–77.
Park, C., Song, Y., Kang, Il-M, Shim, J., Chung, D., Park, C.-S., 2017. Metasomatic changes during periodic fluid flux recorded in grandite garnet from the Weondong W-skarn deposit, South Korea. Chem. Geol. 451, 135–153.
Pawlowsky-Glahn, V., Egozcue, J.J., 2001. Geometric approach to statistical analysis on the simplex. Stoch. Environ. Res. Risk. Assess. 15 (5), 384–398.
Pawlowsky-Glahn, V., Egozcue, J.J., 2006. Compositional data and their analysis: an introduction. In: Buccianti, A., Mateu-Figueras, G., Pawlowsky-Glahn, V. (Eds.), Compositional Data Analysis in the Geosciences: From Theory to Practice. Geological Society, London, Special Publications Vol. 264. pp. 1–10.
Pawlowsky-Glahn, V., Egozcue, J.J., Tolosana-Delgado, R., 2015. Modeling and Analysis of Compositional Data. John Wiley & Sons, Ltd.pp. 247.
Pearce, J.A., Cann, J.R., 1973. Tectonic setting of basic volcanic rocks determined using trace element analyses. Earth Planet. Sci. Lett. 19 (2), 290–300.
Pearson, K., 1897. Mathematical contributions to the theory of evolution. On a form of

spurious correlation which may arise when indices are used in the measurement of organs. In: Proceedings of the Royal Society of London, LX, pp. 489–502.
Plank, T., 2014. The Chemical Composition of Subducting Sediments. In: Rudnick, R.L. (Ed.), Treatise on Geochemistry, second ed. Volume 4. Elsevier, Amsterdam, pp. 607–629.
Polat, A., Hofmann, A.W., 2003. Alteration and geochemical patterns in the 3.7-3.8 Ga Isua greenstone belt, West Greenland. Precambrian Res. 126, 197–218.
Polat, A., Hofmann, A.W., Münker, C., Regelous, M., Appel, P.W.U., 2003. Contrasting geochemical patterns in the 3.7-3.8 Ga pillow basalt cores and rims, Isua greenstone belt, Southwest Greenland: implications for postmagmatic alteration processes. Geochim. Cosmochim. Acta 67, 441–457.
Pownceby, M.I., Johnson, C., 2014. Geometallurgy of Australian uranium deposits. Ore Geol. Rev. 56, 25–44.
Rasmussen, J.C., Hoag, C., Horstman, K.C., 2012. Geology of the Northern Santa Rita Mountains, Arizona. Arizona Geological Society Fall Trippp. 24.
Rudnick, R.L., Gao, S., 2003. Composition of the continental crust. In: Holland, H.D., Turekian, K.K. (Eds.), Treatise on Geochemistry. Volume 3. Elsevier, Amsterdam, pp. 1–64.
Sinha, P., Lambert, M.B., Trumbull, V.L., 2006. Evaluation of statistical methods for left-censored environmental data with nonuniform detection limits. Environ. Toxicol. Chem. 25 (9), 2533–2540.
Soloviev, S.G., Kryazhev, S., 2017. Geology, mineralization, and fluid inclusion characteristics of the Chorukh-Dairon W-Mo-Cu skarn deposit in the Middle Tien Shan, Northern Tajikistan. Ore Geol. Rev. 80, 79–102.
Staudigel, H., Plank, T., White, B., Schmincke, H.-U., 1996. Geochemical fluxes during sea floor alteration of the basaltic upper oceanic crust: DSDP sites 417 and 418. In: Bebout, G.E., Scholl, S.W., Kirby, S.H., Platt, J.P. (Eds.), Subduction: Top to bottom: American Geophysical Union, Washington, pp. 19–38.
Taylor, S.R., McLennan, S.M., 1985. The Continental Crust: Its Composition and Evolution. Blackwell, Oxford, pp. 312.
Tolosana-Delgado, R., Otero, N., Pawlowsky-Glahn, V., 2005. Some basic concepts of compositional geometry. Math. Geol. 37 (7), 673–680.
van den Boogaart, K.G., Tolosana-Delgado, R., 2013. Analyzing Compositional Data with R. Springerpp. 258.
van den Boogaart, K.G., Tolosana-Delgado, R., Bren, M., 2015. R Package "compositions", Version 1.40–1. Compositional Data Analysispp. 264.
von Eynatten, H., Pawlowsky-Glahn, V., Egozcue, J.J., 2002. Understanding perturbation on the simplex: a simple method to better visualize and interpret compositional data in ternary diagrams. Math. Geol. 34 (3), 249–257.
Wang, S.-W., Zhou, T.-F., Yuan, F., Fan, Y., Zhang, L.-J., Song, Y.-L., 2015a. Petrogenesis of Dongguashan skarn-porphyry Cu-Au deposit related intrusion in the Tongling district, eastern China: Geochronological, mineralogical, geochemical and Hf isotopic evidence. Ore Geol. Rev. 64, 53–70.
Wang, Y., Peng, Y., Nicholson, T., Lauten, R.A., 2015b. The different effects of bentonite and kaolin on copper flotation. Appl. Clay Sci. 114, 48–52.
Wang, Y., Lauten, R.A., Peng, Y., 2016a. The effect of biopolymer dispersants on copper flotation in the presence of kaolinite. Miner. Eng. 96-97, 123–129.
Wang, Y., Peng, Y., Nicholson, T., Lauten, R.A., 2016b. The role of cations in copper flotation in the presence of bentonite. Miner. Eng. 96-97, 108–112.
Wood, D.A., 1980. The application of a Th-Hf-Ta diagram to problems of tectonomagmatic classification and to establishing the nature of crustal contamination of basaltic lavas of the British Tertiary Volcanic Province. Earth Planet. Sci. Lett. 50 (1), 11–30.
Yang, L.-Q., Deng, J., Gao, X., He, W.-Y., Meng, J.-Y., Santosh, M., Yu, H.-J., Yang, Z., Wang, D., 2017. Timing of formation and origin of the Tongchanggou porphyry-skarn deposit: implications for Late Cretaceous Mo-Cu metallogenesis in the southern Yidun Terrane, SE Tibetan Plateau. Ore Geol. Rev. 81, 1015–1032.
Yildirim, B.G., Bradshaw, D., Powell, M., Evans, C., Clark, A., 2014. Development of an effective and practical process alteration index (PAI) for predicting metallurgical responses of Cu porphyries. Miner. Eng. 69, 91–96.
Zhou, Z., Mao, J., Che, H., Ouyang, H., Ma, X., 2017. Metallogeny of the Handagai skarn Fe-Cu deposit, northern great Xing'an range, NE China: Constraints on fluid inclusions and skarn genesis. Ore Geol. Rev. 80, 623–644.